A Speed and Flux Observer of Induction Motor Based on Extended Kalman Filter and Markov Chain

Zhonggang Yin, *Member, IEEE*, Guoyin Li, Yanqing Zhang, Jing Liu, Xiangdong Sun, and Yanru Zhong

***Abstract*—To improve the performance of sensorless induction motor (IM) drives, an adaptive speed and flux estimation method based on the multiple-model extended Kalman filter (EKF) with Markov chain for IMs is proposed in this paper. In this algorithm, the multiple model EKF for speed and flux estimation is established, and the transition of the models obeys the Markov chain and the estimation value is obtained by mixing the outputs of different models in different weightings, and the calculation of the weighting is researched. Simultaneously, the transition probability can be continuously self-tuned by the residual sequence, the prior information is modified by the posterior information, and the more accurate transition among the models is obtained. Therefore, the proposed method improves the model adaptability to the actual systems and the environmental variations, and reduces the speed estimation error. The correctness and the effectiveness of the proposed method are verified by the simulation and experimental results.**

***Index Terms*—Adaptive speed and flux estimation, induction motor (IM), Markov chain (MC), multiple-model extended Kalman filter (MM-EKF).**

NOMENCLATURE

α, β	Stationary reference frame axes.
d, q	Rotary reference frame axes.
a, b, c	Three-phase reference frame axes.
i_α, i_β	α-axis and β-axis stator currents, A.
i_d, i_q	d-axis and q-axis stator currents, A.
i_a, i_b, i_c	a-axis, b-axis, and c-axis stator currents, A.
u_α, u_β	α-axis and β-axis stator voltages, V.
u_d, u_q	d-axis and q-axis stator voltages, V.
ψ_α, ψ_β	α-axis and β-axis rotor flux linkages, Wb.
$V_{\rm dc}$	DC link voltage, V.
$\square^*$	Reference quantity.
θ	Rotor position.
J	Moment of inertia.
ω_{sl}	Slip frequency, rad/s.
ω_r	Angular rotor speed, rad/s.
L_m	Mutual inductance, H.
L_s, L_r	Stator and rotor inductances, H.
$\sigma\,(=1-(L_{\rm m}^2/L_{\rm s}L_{\rm r}))$	Total leakage coefficient.
σ_r	Rotor leakage coefficient.
σ_s	Stator leakage coefficient.
R_s, R_r	Stator and rotor resistances, Ω.
$T_r\,(=L_r/R_r)$	Rotor time constant.
T	Sampling period, μs.
V_k	System noise.
W_k	Measurement noise.
T_L	Rated torque, N·m.
P	Pole pair.
P_N	Rated power, kW.
U_N	Rated voltage, V.
I_N	Rated current, A.
f_N	Rated frequency, Hz.

Manuscript received May 5, 2016; revised September 11, 2016; accepted October 24, 2016. Date of publication November 1, 2016; date of current version April 24, 2017. This work was supported in part by the National Natural Science Foundation of China under Grants 51677150 and 51307139, in part by the Specialized Research Fund of Shaan Xi Province under Grant 2015KJXX-29, and in part by the Industrial Research Projects of Shaan Xi Province under Grant 2014K06-29. Recommended for publication by Associate Editor Y. W. Li.

The authors are with the Xi'an University of Technology, Xi'an 710048, China (e-mail: zhgyin@xaut.edu.cn; liguoyin199@163.com; zhangyanqing029@163.com; jingliu@xaut.edu.cn; sxd1030@xaut.edu.cn; zhongyr@xaut.edu.cn).

Color versions of one or more of the figures in this paper are available online at http://ieeexplore.ieee.org.

Digital Object Identifier 10.1109/TPEL.2016.2623806

I. INTRODUCTION

INDUCTION motors (IM) have many advantageous characteristics, such as the high robustness, the reliability and the low cost compared with dc motors. Installation of speed sensors increases the cost, and also reduces the robustness and the reliability of the IM drives. Therefore, much effort has been focused on the rotor speed estimation to achieve sensorless control. A number of sensorless methods has been proposed, such as artificial neural networks (ANN) [1], model reference adaptive systems (MRAS) [2]–[4], high-frequency signal injection [5], [6], full-order adaptive observer [7]–[9], sliding-mode observer [10], [11] and extended Kalman filter (EKF) [12]–[37].

In [1], a new method based on ANNs applied to the parameter estimation of IM using sensorless vector control is proposed, and the results obtained with the proposed observer are more efficient than the results obtained with the classical one. Orlowska-Kowalska and Dybkowski [2] design a novel MRAS-type to estimate the rotor speed for the vector control IM drive. In [3], a new sensorless internal temperature monitoring method for IM is proposed. An alternative adaptation mechanism for MRAS-based sensorless IM drive is presented in [4]. However, in these studies, with respect to sensorless IM drives, the rotor flux and load torque should be known to realize the sensorless controller. Moreover, these observers usually lose effectiveness or give inaccurate results due to the unobservability at low speeds. Caruana *et al*. [5] use a method to estimate speed based on high-frequency signal injection, and gets good performance. However, some problems need to be

solved, such as sampling frequency of high-frequency current, filter design, and its delay. In [7], [8], and [9], the new design rules for the adaptation of PI gains to satisfy the required performances are proposed. The robustness of the adaptive full-order observer against stator resistance and inductance variations is also investigated, but the speed fluctuation becomes large as the speed decreases. In [10], a fixed-boundary-layer sliding-mode (FBLSM) observer implements a high-performance robust sensorless electric vehicle IM drive requiring only current measurements. The chattering-free FBLSM observer is responsible for accurately estimating speed and rotor flux, even with unknown load torque. In low-speed conditions, it still performs good observability.

Unlike the other methods, EKF takes a stochastic approach to state estimation. In spite of its computational complexity, EKF makes the online state estimation possible while performing identification of parameters in a relatively short time interval, and takes system and measurement noises into account directly. Recently, EKF has been studied widely on the sensorless control of motors. In [12] and [13], the parameter estimator based on EKF is used to estimate the rotor resistance and mutual inductance. The results motivate the utilization of the proposed estimation technique in combination with a variety of control methods for IMs. In [14], the torque and position are estimated by EKF in a stepper motor, and this method can cancel the static error and compensate the load torque variation. Because of the massive calculation with five-order matrix, most research results are only verified by simulations. In order to apply it to practice, a three-order EKF algorithm for flux and speed estimation is proposed in [15]–[17], and the speed and flux linkage are estimated easily. In [18]–[20], EKF is used for speed and flux linkage estimation in direct torque control system, and the experiment results show that the system based on EKF has good performance and applicable value. Indicative applications of nonlinear filters in control problems have been presented in [21], where EKF has been used in state estimation-based condition monitoring of electrohydraulic actuators. In [22] and [23], EKF is used as a speed and position estimator in the vector control system of the IM, which has been implemented as a state observer for IM drives in various configurations. In [24], EKF has been used for estimating the electromagnetic torque of direct-torque controlled brushless dc motors and for implementing a sensorless control scheme. Salvatore *et al*. [25] present a novel sensorless stator-flux-oriented sliding-mode scheme based on an offline-optimized-delayed-state Kalman filter algorithm to estimate the stator-flux components and rotor speed in IMs, and gets good performance. In [26], the application of optimal state estimation and optimal state feedback algorithms based on the EKF for real-time active magnetic bearing control is treated. It is shown that this controller yields improved rotor positioning accuracy, better system dynamics, higher bearing stiffness, and reduced control energy effort compared with the conventionally used proportional-integral-differential control approaches. In [27], EKF has been used to estimate the rotor speed, the rotor flux, and the stator flux, and the stator currents accurately in the vector control system of the IMs, and the small stator current THD is confirmed. Depending on the commanded speed, either the rotor current model or the open-loop stator voltage model is proposed for EKF to achieve better performance in a wide speed range, including the field-weakening region.

However, the noise covariance matrix of EKF is unitary, and the different situation and work modes cannot be adjusted. Moreover, EKF is poorly robust against model uncertainties, which results in inaccuracy of EKF state estimation, and even causes the system to diverge. When the system reaches the stable state, the Kalman gain and the error covariance matrix are limited within a low level, and the tracking ability to the mutations is lost. EKF cannot track these changes fast when the external environment is mutated. In [28], an interacting multiple-model EKF (IMM-EKF) is proposed to solve aforementioned problems, and the influence by gross external disturbance and internal estimated error is reduced based on IMM-EKF. However, the transition probability matrix is fixed, and the transition probability cannot be updated with the change of environment and working conditions in IMM-EKF. The main contribution of this paper is that a novel speed and flux estimation method for IMs based on the multiple-model extended Kalman filter with Markov chain (MC-MM-EKF) is proposed to improve the model adaptability to the actual systems and the environmental variations, and reduce the speed estimation error. With this method, the multiple models are designed to replace the running modes of system, the transition of models obeys Markov chain, and the estimation value is obtained by mixing the outputs of different models in different weightings. Simultaneously, the transition probability can be continuously self-tuned by the residual sequence, the prior information is modified by the posterior information, and the more accurate transition among the models is obtained. The correctness and the effectiveness of the proposed method are demonstrated by the simulation and experimental results.

II. EKF Observer for IM

The system equation and the observer equation are supposed to be linear for Kalman filter. However, the actual system cannot satisfy this supposition. The nonlinear system can approximate the linear system with EKF, and the calculation precision will be enhanced with this algorithm. EKF is formulated as follows:

$$\frac{d\hat{x}}{dt} = A(\hat{x})\hat{x} + Bu + K(y - \hat{y}) \tag{1}$$

$$\hat{y} = H\hat{x} \tag{2}$$

where $\hat{x}$ is set as the state variable, $\hat{y}$ is set as the observation variable, y is the actual measurement value, u is the control variable, $A(\hat{x})$ is the state matrix, B is the input matrix, H is the observation matrix, and K is the gain matrix.

For EKF, some unmeasured variables can be calculated from the measured value. Generally, the stator voltage and stator current are set to be the measured vector, namely $u = u_s$, $y = i_s$. In addition, the other measured vectors contain noise vector V and W

$$\operatorname{cov}(V_k, V_i) = E\{V_k V_i^T\} = \begin{cases} Q, i = k \\ 0, i \neq k \end{cases} \tag{3}$$

$$\operatorname{cov}(W_k, W_i) = E\{W_k W_i^T\} = \begin{cases} R, i = k \\ 0, i \neq k \end{cases} \tag{4}$$

$$\operatorname{cov}(V_k, W_i) = E\{V_k W_i^T\} = 0, \quad \text{for all } i \text{ and } k. \tag{5}$$

Both vector W_k and vector V_k are zero-mean Gaussian white sequences with a zero cross correlation with each other. Q and R are the positive definite matrices. The covariance matrix of system noise Q accounts for the model inaccuracy, the system disturbances, and the noise introduced by the voltage measurements (sensor noise and A/D converter quantization). The covariance matrix of measurement noise R accounts for the measurement noise introduced by the current sensors and A/D quantization.

In order to build a digital system of EKF, make (1) and (2) discrete

$$\hat{x}_{k+1} = A'\hat{x}_k + B'u_{k+1} + K_{k+1}(y - \hat{y}) \tag{6}$$

$$\hat{y}_{k+1} = H_{k+1}\hat{x}_{k+1} \tag{7}$$

where A' and B' are the disperse matrix of the $A(\hat{x})$ and B, respectively. $\tilde{\bullet}$ is the prediction value and $\hat{\bullet}$ is the update value

$$x_k = (\, i_{\alpha,k} \quad i_{\beta,k} \quad \psi_{\alpha,k} \quad \psi_{\beta,k} \quad \omega_{r,k} \quad)^T,$$

$$A' = \begin{bmatrix} 1-\dfrac{T}{T'_{sr}} & 0 & \dfrac{TL_m}{\sigma L_s L_r T_r} & \omega_r \dfrac{TL_m}{\sigma L_s L_r} & 0 \\ 0 & 1-\dfrac{T}{T'_{sr}} & -\omega_r \dfrac{TL_m}{\sigma L_s L_r} & \dfrac{TL_m}{\sigma L_s L_r T_r} & 0 \\ \dfrac{TL_m}{T_r} & 0 & 1-\dfrac{T}{T_r} & -T\omega_r & 0 \\ 0 & \dfrac{TL_m}{T_r} & T\omega_r & 1-\dfrac{T}{T_r} & 0 \\ 0 & 0 & 0 & 0 & 1 \end{bmatrix},$$

$$B' = \begin{bmatrix} \dfrac{T}{\sigma L_s} & 0 \\ 0 & \dfrac{T}{\sigma L_s} \\ 0 & 0 \\ 0 & 0 \\ 0 & 0 \end{bmatrix}, \quad H_k = \begin{bmatrix} 1 & 0 & 0 & 0 & 0 \\ 0 & 1 & 0 & 0 & 0 \end{bmatrix},$$

$$u_k = (\, u_{\alpha,k} \; u_{\beta,k})^T, \; T'_{sr} = \sigma L_s / R_{sr},$$

$$R_{sr} = R_s + (L_m/L_r)^2 R_r, \; T_r = L_r/R_r.$$

In EKF, the deviation is used to feedback correction, and the specific process includes the following steps [26]–[33]:

1) Prediction of the state variable

$$\tilde{x}_{k+1} = A'\hat{x}_k + B'u_{k+1}. \tag{8}$$

2) Prediction of the error covariance matrix $\tilde{P}_{k+1}$

$$\tilde{P}_{k+1} = G_{k+1}\hat{P}_k G_{k+1}^T + Q_{k+1} \tag{9}$$

where, see the unnumbered equation shown at the bottom of the page.

3) Calculation of the Kalman filter gain matrix K_{k+1}

$$K_{k+1} = \tilde{P}_{k+1}H_{k+1}^T \Big(H_{k+1}\tilde{P}_{k+1}H_{k+1}^T + R_{k+1} \Big)^{-1}. \tag{10}$$

4) Update of the state prediction variable

$$\hat{x}_{k+1} = \tilde{x}_{k+1} + K_{k+1}(y_{k+1} - H_{k+1}\tilde{x}_{k+1}). \tag{11}$$

5) Update of the error covariance matrix $\hat{P}_{k+1}$

$$\hat{P}_{k+1} = (I - K_{k+1}H_{k+1})\tilde{P}_{k+1}. \tag{12}$$

III. MC-MM-EKF Observer

A. Multiple-Model EKF

In the single model extended Kalman filter (SM-EKF), the noise covariance matrix is unitary so that it cannot adjust different situation and work modes. Moreover, EKF is poorly robust against model uncertainties. When the motor running state does not conform to the model, there is a greater speed estimation error. A multiple-model EKF which designs multiple EKF model based on the different noise covariance matrices is proposed here to solve the above problem. Take the range of covariance in consideration, EKF model is established with different covariance matrix, such as Q1, Q2 . . . Qn. Every model has the same algorithm with SM-EKF and the different value is obtained, and the output of the system is added with different weighting, as shown in Fig. 1.

v_k^i is the residual sequence of model i, it can be calculated as follows:

$$v_k^i = y_k - H_k^i \tilde{x}_k^i. \tag{13}$$

The residual covariance matrix is given by

$$S_k^i = H_k^i \tilde{P}_k^i H_k^{iT} + R_k^i. \tag{14}$$

$$G_{k+1} = \left(\frac{\partial}{\partial x}(A'x + B'u) \right) |_{x=\tilde{x}_{k+1}} \begin{bmatrix} 1-\dfrac{T}{T'_{sr}} & 0 & \dfrac{TL_m}{\sigma L_s L_r T_r} & \tilde{\omega}_{r,k+1}\dfrac{TL_m}{\sigma L_s L_r} & \dfrac{TL_m}{\sigma L_s L_r}\tilde{\psi}_{\beta,k+1} \\ 0 & -\dfrac{T}{T'_{sr}} & -\tilde{\omega}_{r,k+1}\dfrac{TL_m}{\sigma L_s L_r} & \dfrac{TL_m}{\sigma L_s L_r T_r} & -\dfrac{TL_m}{\sigma L_s L_r}\tilde{\psi}_{\alpha,k+1} \\ \dfrac{TL_m}{T_r} & 0 & 1-\dfrac{T}{T_r} & -T\tilde{\omega}_{r,k+1} & -T\tilde{\psi}_{\beta,k+1} \\ 0 & \dfrac{TL_m}{T_r} & T\tilde{\omega}_{r,k+1} & 1-\dfrac{T}{T_r} & T\tilde{\psi}_{\alpha,k+1} \\ 0 & 0 & 0 & 0 & 1 \end{bmatrix}$$

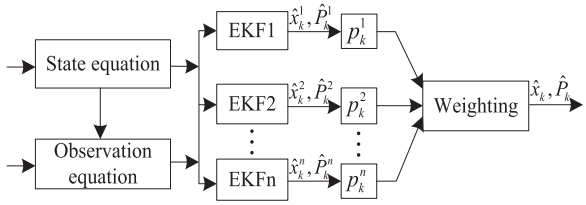

Fig. 1. Structure of the MM-EKF algorithm.

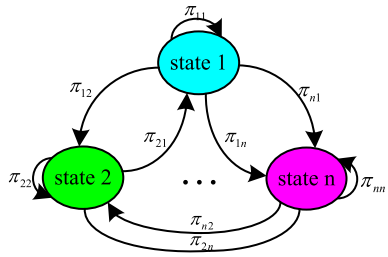

Fig. 2. Structure of the Markov chain.

According to the residual and covariance matrix, the likelihood function is shown as follows:

$$f_i(\bullet) = N(v_k^i : 0, S_k^i) \tag{15}$$

where $f_i(\bullet)$ denotes the likelihood of model i.

According to the fuzzy inference principle, the normalized constant is obtained as follows:

$$c_k = \sum_{i=1}^{n} f_i(\bullet) \times p_k^i. \tag{16}$$

The weighting is calculated as follows:

$$p_k^i = \frac{f_i(\bullet) \times p_{k-1}^i}{c_k}. \tag{17}$$

The final value and error covariance matrix are summed up with all models in different weighting

$$\hat{x}_k = \sum_{i=1}^{n} \hat{x}_k^i \times p_k^i \tag{18}$$

$$\hat{P}_k = \sum_{i=1}^{n} \hat{P}_k^i \times p_k^i. \tag{19}$$

In this algorithm, there is no interaction among the models of system. Therefore, it is a static multiple model algorithm, which has good performance for the time-invariant and structure-fixing systems. However, the motor control system is a highly complex and strong coupling system, and it is easily affected by the internal factors and external environment. When the motor running state changes seriously, it will make the speed estimation wrong, and even cause the system to diverge.

B. Multiple-Model EKF Based on Markov Chain

According to the above analysis, the interaction among the models is added based on multiple-model EKF algorithm. Compared with MM-EKF, the IMM-EKF has better adaptive ability, which can effectively avoid switching among different noise models too conservatively, and take consideration of the system optimality. In IMM, the switching of the models is characterized quantitatively with switching probability, and the estimated precision is not only related to the modeling accuracy, but also directly related to the input interaction estimation, and the switching probability has great effects on input interaction.

However, the interaction parameters selected by the prior information is a tradeoff between mode switching and nonswitching. The switching speed and the filtering accuracy of the models are affected by the lag of probability and noise. A multiple-model EKF with Markov chain is proposed in this paper. It is assumed that the transition among the different models obeys the Markov chain of finite state, and the structure of Markov chain is shown in Fig. 2. Simultaneously, the measurement information in the residual sequence is used to update the model transition probability, and the prior information is modified by posterior information, which makes the transition probability and the models coincident with the actual situation. At last, MC-MM-EKF gives the final result by fusion based on the likelihood function of every model. Thus, the filtering accuracy and anti-interference performance are improved, and the influence of the uncertain prior information is weakened. The proposed method shows more robust against the model uncertainties or the time-varying parameter systems, and it has better tracking ability to the mutations and the slow changes. Therefore, the proposed method improves the model adaptability to the actual systems and environmental variations, and reduces the speed estimation error. The proof of convergence for MC-MM-EKF is shown in the Appendix, and the structure of MC-MM-EKF is shown in Fig. 3.

The prior Markov transition probability of the system is as follows:

$$\pi_{\mathrm{ij}} = \begin{bmatrix} 0.8 & 0.1 & 0.1 \\ 0.1 & 0.8 & 0.1 \\ 0.1 & 0.1 & 0.8 \end{bmatrix}$$

where π_{ij} is the transition probability from the model i to the model j, and u_{k+1}^i is the model matching probability.

C. Update of Markov Transition Probability

The residual of filter is observed directly, and it can be used as a reference for the filter performance by observing the covariance of the residual sequence. Actually, the measurement information is in the residual, and the hybrid residual sequence of MC-MM-EKF can be calculated as follows:

$$\nu_{k+1}^{\mathrm{ij}} = y_{k+1} - H_{k+1}^j (A_j' \hat{x}_k^i + B_j' u_k). \tag{20}$$

The residual covariance matrix is as follows:

$$\begin{aligned} S_{k+1}^{\mathrm{ij}} &= E\left\{ v_{k+1}^{\mathrm{ij}} \bullet v_{k+1}^{\mathrm{ij}T} | m_{k+1}^j, Y_{k+1} \right\} \\ &= R_{k+1}^j + H_{k+1}^j A_j' \hat{P}_{k+1}^i A_j'^T H_{k+1}^{jT} \\ &\quad + H_{k+1}^j D_k^{\mathrm{ij}} H_{k+1}^{jT} \end{aligned} \tag{21}$$

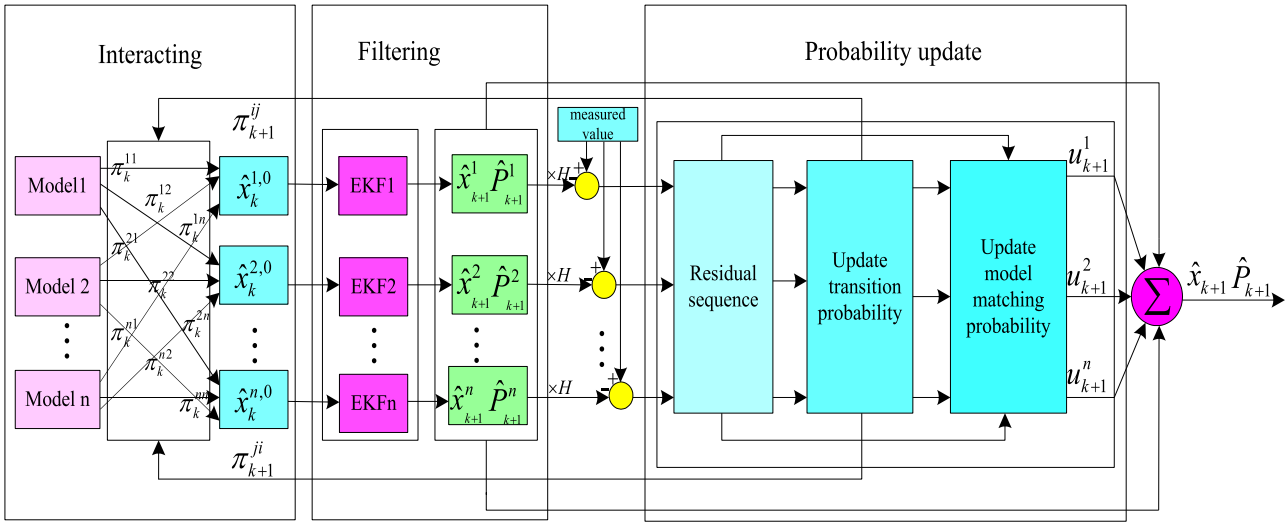

Fig. 3. Structure of the multiple-model extended Kalman filter based on the Markov chain algorithm.

where m_k^j indicates that model i matches with the current running mode, Y_{k+1} is the observation set, and $Y_{k+1} = \{y_{k+1}^1, y_{k+1}^2, \cdots, y_{k+1}^n\}$.

According to the residual sequence, the likelihood function is given by

$$\Lambda_{k+1}^{ij} = N[\nu_{k+1}^{ij} : 0, S_{k+1}^{ij}] = \exp\left\{-0.5\nu_{k+1}^{ijT} S_{k+1}^{ij-1} \nu_{k+1}^{ij}\right\} / \sqrt{2\pi \left|S_{k+1}^{ij}\right|} \quad (22)$$

where D_k^{ij} is the process noise covariance matrix, and it can be calculated as follows:

$$D_k^{ij} = E\left\{Q_k | m_k^i, m_{k+1}^j, Y_{k+1}\right\}. \quad (23)$$

The adaptive transition probability based on the measurement information is given by

$$\pi_{k+1}^{ij} = P\left\{m_{k+1}^j | m_k^i, Y_{k+1}\right\} = \frac{\Lambda_{k+1}^{ij} \bullet P\left\{m_{k+1}^j | m_k^i, Y_{k+1}\right\}}{P\left\{y_{k+1} | m_k^i, Y_k\right\}}. \quad (24)$$

The observation set Y_k only contains model matching information before time k, and thus

$$P\left\{m_{k+1}^j | m_k^i, Y_{k+1}\right\} = P\left\{m_{k+1}^j | m_k^i\right\} = \pi_k^{ij}. \quad (25)$$

Equation (21) is rewritten as follows:

$$\pi_{k+1}^{ij} = \Lambda_{k+1}^{ij} \bullet \pi_k^{ij} / \eta \quad (26)$$

where

$$\eta = \sum_{i=1}^{n} \Lambda_{k+1}^{ij} \bullet \pi_k^{ij}. \quad (27)$$

The posterior Markov transition probability is obtained based on the above method, and it contains more accurate distribution information of model transition probability. π_{k+1}^{ij} is used as transition probability next time, which makes model switching more accurate and reduces the influence of prior information. Therefore, the fusion precision is improved.

D. Mechanism of Process Noise Covariance Matrix

When the disturbance mechanism is clear, the variance of independent disturbance sources is a diagonal matrix. If every model is designed independently, there will be more parameters. The multiple-model modeling method has generalization capacity, but it appears more requirement of parameter design, which provides the possibility to introduce new information to implement the parameter design and optimization online.

D_k^{ij} is the process noise variance based on the model which is known at two moments, and the basic idea is that it establishes the relationship of noise variance between model state maintaining and switching by the Bayes total probability. Because the model mismatching difference is larger in process of the state with maintaining and switching, the process noise variances are designed respectively. When the running mode of the system is known, D_k^{ij} is unrelated with the observation set Y_{k+1}, and (23) can be rewritten as follows:

$$D_k^{ij} = E\left\{Q_k | m_k^i, m_{k+1}^j\right\}. \quad (28)$$

There is always some inertia in the filtering system, and the identification of model has delay with the mask of noise, which causes the process noise of model to show nonstationarity. Generally, $D_k^{ij} >> D_k^{jj}$ and D_k^{ii}.

E. Steps of MC-MM-EKF for IM

Step 1: Posterior estimation for Markov transition probability

Take $\hat{x}_k^i$,$\hat{P}_k^i$ into the model j with filtering, the posterior transition probability can be calculated from (20)–(27).

Step 2: Input interaction

In this section, individual filters are mixed according to the predicted model probabilities. The predicted model probability is given by the model probability in the previous cycle u_k^i and the probability that a transition from state i to state j occurs π_{ij},

the initial mixing state $\hat{x}_k^{\mathrm{oj}}$ and the initial mixing covariance $\hat{P}_k^{\mathrm{oj}}$ are given by

$$\hat{x}_k^{\mathrm{oj}} = \sum_{i=1}^{n} u_k^{\mathrm{ij}} \hat{x}_k^i \tag{29}$$

$$\hat{P}_k^{\mathrm{oj}} = \sum_{j=1}^{n} u_k^{\mathrm{ij}} \left\{ \hat{P}_k^j + \left[\hat{x}_k^j - \hat{x}_k^{\mathrm{oj}} \right] \bullet \left[\hat{x}_k^j - \hat{x}_k^{\mathrm{oj}} \right]^T \right\} \tag{30}$$

$$u_k^{\mathrm{ij}} = \pi_k^{\mathrm{ij}} u_k^i / \bar{\varsigma}_k^i \tag{31}$$

$$\bar{\varsigma}_k^j = \sum_{i=1}^{n} \pi_{k+1}^{\mathrm{ij}} u_k^i. \tag{32}$$

Step 3: Prediction of the state

Use $\hat{x}_k^{\mathrm{oj}}$ and $\hat{P}_k^{\mathrm{oj}}$ based on EKF to get state $\hat{x}_{k+1}^j$, covariance $\hat{P}_{k+1}^j$ and residual v_{k+1}^j.

Step 4: Update of the model matching probability

The likelihood function of model *j* is as follows:

$$\begin{aligned} \Lambda_{k+1}^j &= N\left[\nu_{k+1}^j : 0, S_{k+1}^j\right] \\ &= \exp\left\{-0.5 \nu_{k+1}^{jT} S_{k+1}^{j-1} \nu_{k+1}^j\right\} / \sqrt{2\pi \left| S_{k+1}^j \right|}. \end{aligned} \tag{33}$$

Using the Bayes rule, the model matching probability is given by

$$u_{k+1}^j = \Lambda_{k+1}^j \bar{\varsigma}_j / \varsigma \tag{34}$$

$$\varsigma = \sum_{j=1}^{n} \Lambda_j (k+1) \bar{\varsigma}_j. \tag{35}$$

Step 5: Combination

According to the model matching probability, the mean and covariance of the combined state estimation are as follows:

$$\hat{x}_{k+1} = \sum_{j=1}^{n} \hat{x}_{k+1}^j u_{k+1}^j \tag{36}$$

$$\begin{aligned} \hat{P}_{k+1} = \sum_{j=1}^{n} u_{k+1}^j \Big\{ & P_{k+1}^j + \left[\hat{x}_{k+1}^j - \hat{x}_{k+1} \right] \\ & \bullet \left[\hat{x}_{k+1}^j - \hat{x}_{k+1} \right]^T \Big\}. \end{aligned} \tag{37}$$

It is the essence of the sensorless vector control that the motor speed is not acquired by mechanical sensor, but rather by software in the speed regulating system. The block diagram of the sensorless vector control system for IM is shown in Fig. 4.

The voltage and phase current of motor are transformed to α–β coordinate system. The voltage and current based on -α-β coordinate system are the inputs of the MC-MM-EKF estimator. The rotor speed is estimated to feedback the PI controller. The control voltages ($u_\alpha*$, $u_\beta*$) are transformed to u_d and u_q which are the outputs of the PI controller. At last, the outputs of SVPWM are loaded to a PWM inverter to regulate the IMs. The outputs are the speed, the current, and flux based on an α–β coordinate system.

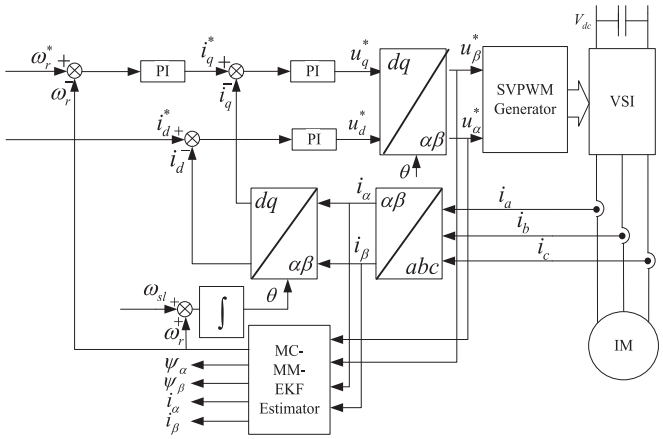

Fig. 4. Block frame of sensorless vector control based on MC-MM-EKF.

TABLE I
MOTOR PARAMETERS

P_N	1.1 kW	R_s	5.27 Ω
U_N	380 V	R_r	5.07 Ω
I_N	2.7 A	L_m	0.421 H
n_N	1410 r/min	L_s	0.423 H
J	0.02 kg m^2	L_r	0.479 H
f_N	50 Hz	P	2

IV. SIMULATION RESULTS

The simulation is carried out by MATLAB/Simulink. In the simulation, the parameters of the IM are shown in Table I. The covariance matrices *Q* and *R* are taken to be diagonal. If a large value of matrix *R* is used, the transient response decreases but the state is well estimated in steady state. As shown in (10), the matrices *K* and *R* are inversely proportional. Therefore, the value of *K* becomes weak in order to give more accuracy to the estimation of the state. Otherwise, overshoot in the transient response and noises in the steady-state response are obtained. In both cases, *R* acts on the transient response and in the steady-state response because its value is constant in the EKE algorithm. The covariance matrix *Q* represents the noises on the system due to the modeling errors. From (9) and (10), the matrix *K* is proportional to matrix *Q*. Then, it has an opposite effect of that of *R*. Under the premise to ensure convergence, the choice of every value of these matrices is done according to the dynamics of the state variables and performance index. In the design phase, some engineering works should be required for MC-MM-EKF. First, the calculation and the procedure of MC-MM-EKF are relatively large. Therefore, the selection of microprocessor is important, and the high-performance microprocessor should be selected to ensure execution efficiency. Second, defining the number of models should be required for MC-MM-EKF. The performance of the algorithm will be affected by the selection of the model set. The model set is so small that the running modes may not be contained. The precision can be improved by increasing the number of models, and the amount of calculation also increases. Moreover, the model competition will be introduced owe to the use of too many models, which leads the algorithm performance

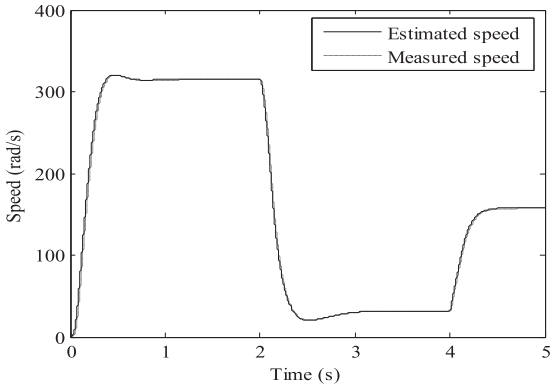

Fig. 5. Comparison of simulation result based on MC-MM-EKF.

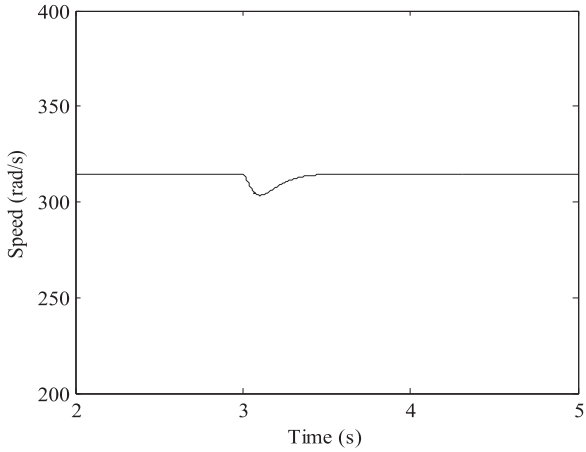

Fig. 6. Speed response when sudden load is added.

to be affected. Accordingly, the performance of the algorithm will be reduced. Therefore, many factors in practice should be considered, such as work conditions, the execution time of program, the precision, and so on. In this paper, three models are set, considering the working conditions and the performance of CPU. The value of the Q and R matrices for EKF are as follows:

$$R = \text{diag}\,[0.1, 0.1],$$

$$Q = \text{diag}\,[2\times10^{-2}, 2\times10^{-2}, 2\times10^{-3}, 2\times10^{-3}, 1].$$

The initial value of u for MC-MM-EKF is $u = [0.97\ 0.015\ 0.015]$. The value of the Q and R matrices for IMM-EKF and MC-MM-EKF are as follows:

Model 1:

$$R_1 = \text{diag}\,[0.01, 0.01]$$

$$Q_1 = \text{diag}\,[5\times10^{-3}, 5\times10^{-3}, 5\times10^{-4}, 5\times10^{-4}, 0.1].$$

Model 2:

$$R_2 = \text{diag}\,[0.1, 0.1]$$

$$Q_2 = \text{diag}\,[2\times10^{-2}, 2\times10^{-2}, 3\times10^{-3}, 3\times10^{-3}, 1].$$

Model 3:

$$R_3 = \text{diag}\,[10, 10]$$

$$Q_3 = \text{diag}\,[5\times10^{-1}, 5\times10^{-1}, 2\times10^{-2}, 2\times10^{-2}, 10].$$

The setting frequency in the simulation is given as follows: the initial frequency is set as 50 Hz. At second second, the frequency is set as 5 Hz. At fourth second, the frequency is set as 25 Hz. The simulation results of speed comparison based on MC-MM-EKF is shown in Fig. 5. It indicates that MC-MM-EKF has good tracking performance and a stable state.

Fig. 6 shows the speed response when sudden load is added. The motor is running with no load at the starting time. At the third second, a sudden load of 10 Nm is added. Because of the sudden load, the speed drops to 300 rad/s, and 0.4 s later, the speed tracks the given speed again. It shows that the good dynamic properties of the speed estimator are based on MC-MM-EKF.

A. With Gross External Error

In order to test the anti-error ability of MC-MM-EKF, a disturbance pulse which valued 2 A is added to i_α based on EKF, IMM-EKF, and MC-MM-EKF. The given frequency speeds up from 0 to 50 Hz in first 0.5 s, runs in 50 Hz for 5 s, and speeds down to 5 Hz. As shown in Fig. 7, EKF has a large estimation error when the gross external disturbance occurs with the largest error of 30 rad/s at rated speed, 35 rad/s at speed down, and 20 rad/s at low speed. IMM-EKF has better anti-error ability, and the largest estimated error is 10 rad/s at rated speed, 13 rad/s at speed down, and 10 rad/s at low speed.MC-MM-EKF has the best anti-error ability, and the largest estimated error is 5 rad/s at rated speed, 8 rad/s at speed down, and 6 rad/s at low speed. Therefore, the MC-MM-EKF has better anti-error ability than EKF and IMM-EKF.

Fig. 8 presents the comparison of the estimated flux. It is shown that flux linkage based on EKF and IMM-EKF has a larger fluctuation, compared with MC-MM-EKF.

B. With Gross Estimation Error

An error vector which is $[0\ 1\ 0\ 0\ 0]^{\mathrm{T}}$ is added to x. Speed estimated error based on EKF, IMM-EKF, and MC-MM-EKF is shown in Fig. 9. As it is presented, EKF has a large estimation error when the gross estimation error occurs with the largest error of 30 rad/s at rated speed, 40 rad/s at speed down, and 25 rad/s at low speed. IMM-EKF has better anti-estimation-error ability, and the largest estimated error is 6 rad/s at rated speed, 11 rad/s at speed down, and 6 rad/s at low speed. MC-MM-EKF has the best anti-estimation-error ability, and the largest estimated error is 3.5 rad/s at rated speed, 6 rad/s at speed down, and 3 rad/s at low speed. Therefore, MC-MM-EKF has better anti-estimation-error ability than EKF and IMM-EKF.

Fig. 10 presents the comparison of the estimated flux. It is shown that flux linkage based on EKF has the largest fluctuation, and flux linkage based on IMM-EKF also has a larger fluctuation, but the fluctuation of the estimated flux linkage based on MC-MM-EKF is much smaller.

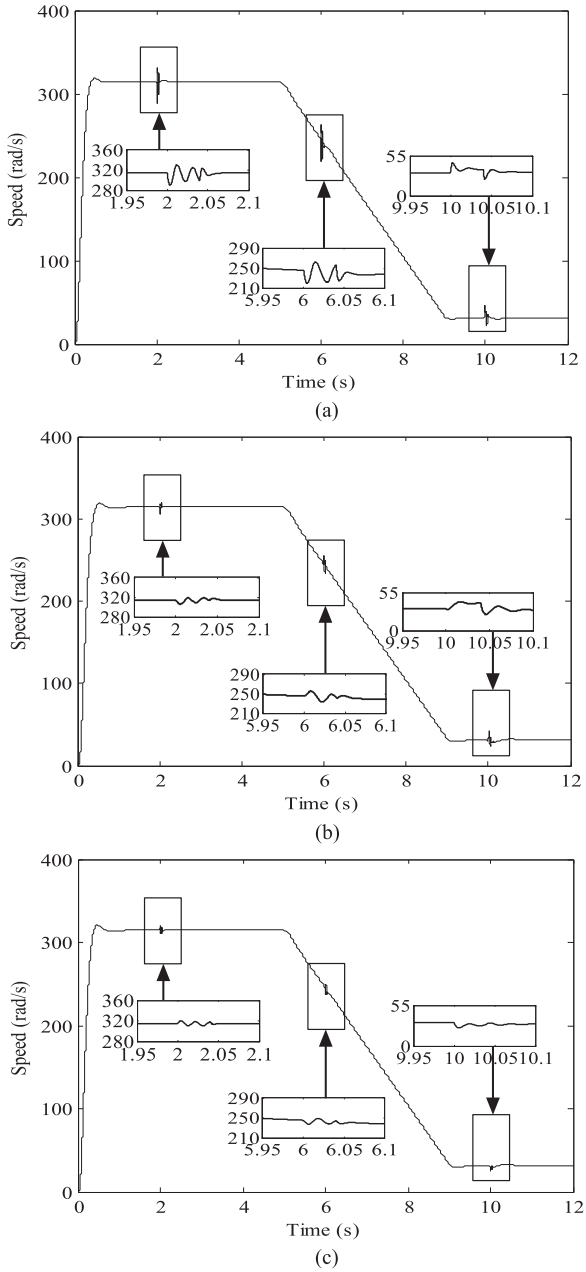

Fig. 7. Comparison of the estimated speed with gross external error. (a) EKF. (b) IMM-EKF. (c) MC-MM-EKF.

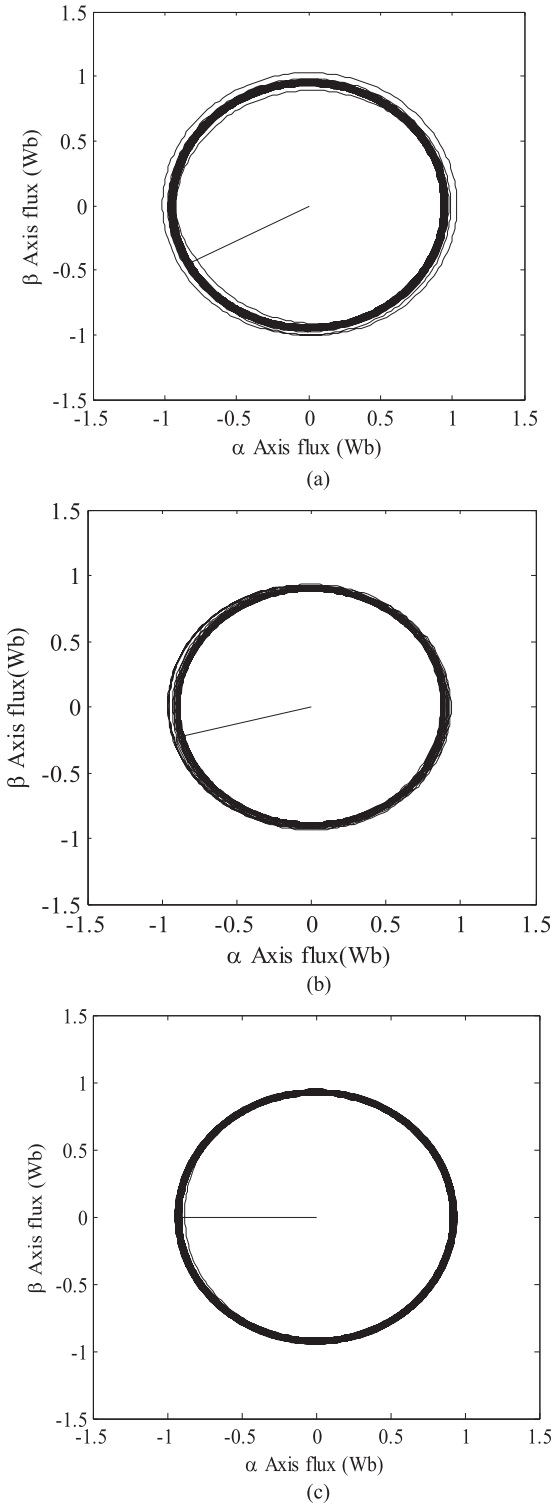

Fig. 8. Comparison of the estimated flux linkage with gross external error. (a) EKF. (b) IMM-EKF. (c) MC-MM-EKF.

V. Experimental Results

The above speed estimation methods are implemented at the experimental platform based on TMS320F28335, and the clock frequency of TMS320F28335 is 150 MHz. The motor parameters are shown in Table I, and the experimental platform is shown in Fig. 11. The value of Q, R, and u is the same as in the simulation. The system hardware consists of an IM, an IM inverter, a loading system, and an oscilloscope. The stator voltage, the stator current, and the rotor speed are measured by the hall effect voltage sensor, the hall effect current sensor, and the photoelectric coder, respectively. The type of the encoder is OMRON: E6C2-CWZ6C, and the encoder resolution is 1024 P/R. The system software process includes initialization, main loop, fault protection, PWM interrupt, etc. The period of the PWM interrupt is 250 μs, and the main functions include coordinate transformation, MC-MM-EKF algorithm, dead time compensation, SVPWM generation, etc. The execution time of traditional EKF is 50 μs, the execution time of IMM-EKF is 155 μs, and the execution time of MC-MM-EKF is 160 μs.

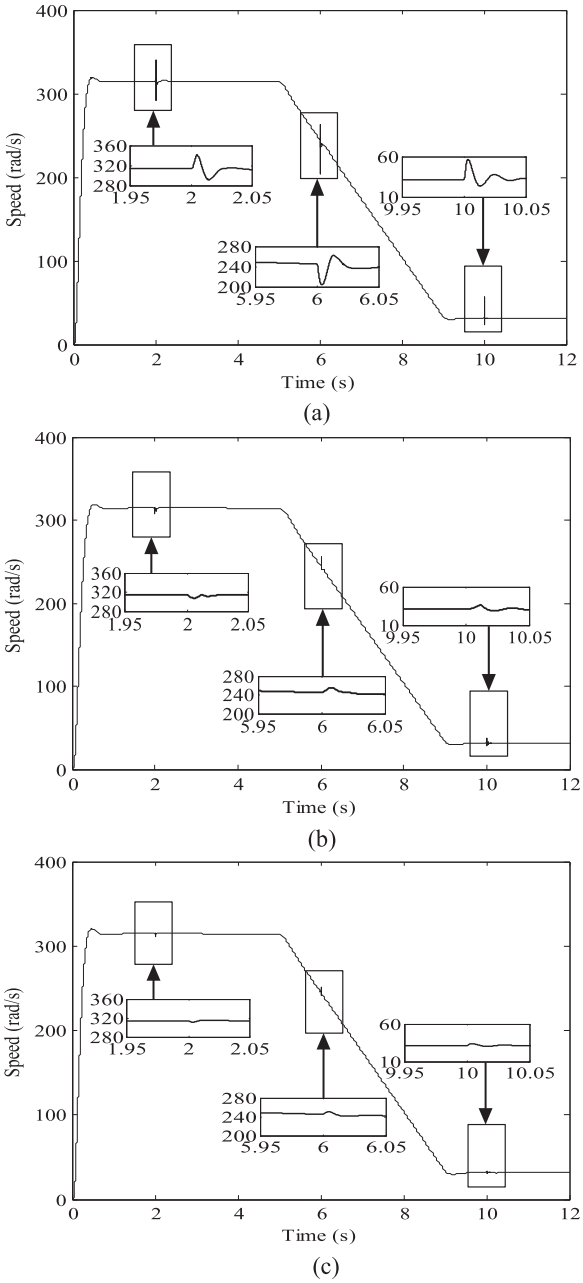

Fig. 9. Comparison of the estimated speed with gross estimation error. (a) EKF. (b) IMM-EKF. (c) MC-MM-EKF.

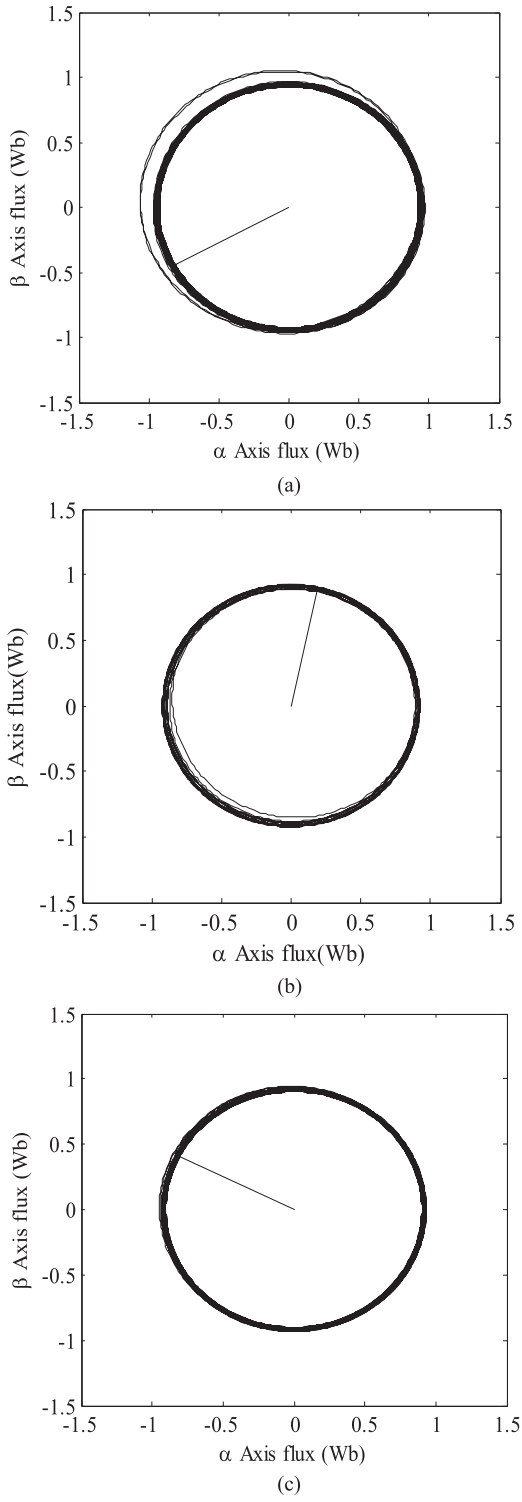

Fig. 10. Comparison of the estimated flux linkage. (a) EKF. (b) IMM-EKF. (c) MC-MM-EKF.

A. Experimental Verification for Speed Estimation During Full Speed and Low Speed

When the motor runs at different speed, the experimental results based on MC-MM-EKF are shown in Fig. 12. From top to bottom, the rotor speed, the estimated speed, and the speed estimation error are given, respectively. It can be seen that the motor runs at six stages, including 2*pi*, 40*pi*, 80*pi*, 100*pi*, 60*pi*, and 20*pi* rad/s, respectively, which contains the full range of running speed, it indicates that the proposed method has good tracking performance.

Fig. 13 shows the estimated speed response based on MC-MM-EKF when the given speed ranges from $+2pi$ to $+10pi$ rad/s. From top to bottom, the rotor speed, the estimated speed, and the speed estimation error are given, respectively. It presents that MC-MM-EKF has good tracking performance during the low-speed range.

Fig. 14 shows that the speed estimation performance based on MC-MM-EKF when speed-sensor fails at 100*pi* rad/s with

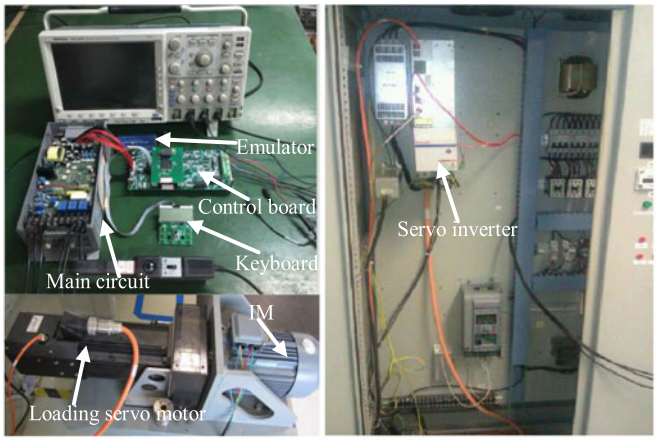

Fig. 11. Experimental platform.

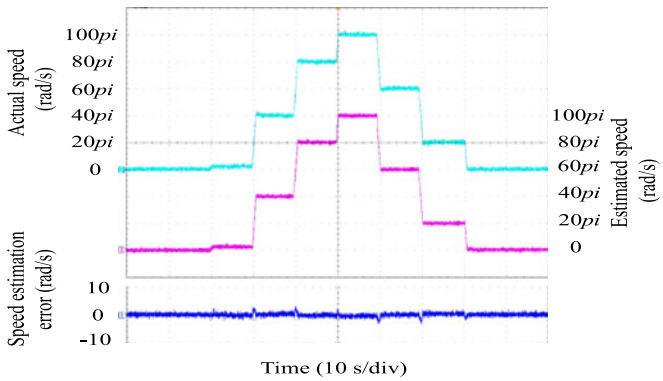

Fig. 12. Speed tracking performance in whole operation based on MC-MM-EKF.

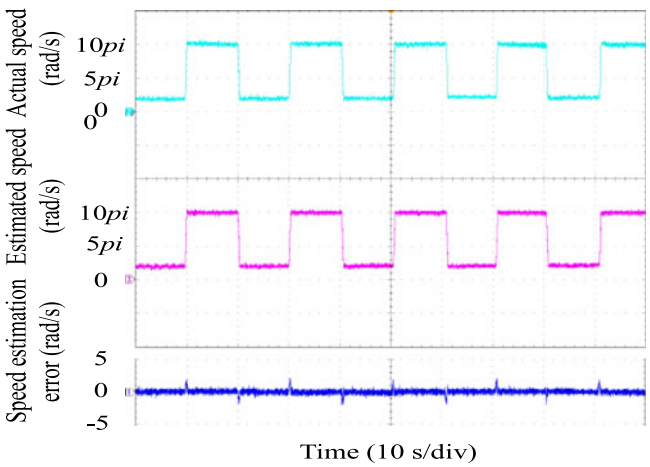

Fig. 13. Speed tracking performance when the given speed ranges from $+2pi$ to $+10pi$ rad/s.

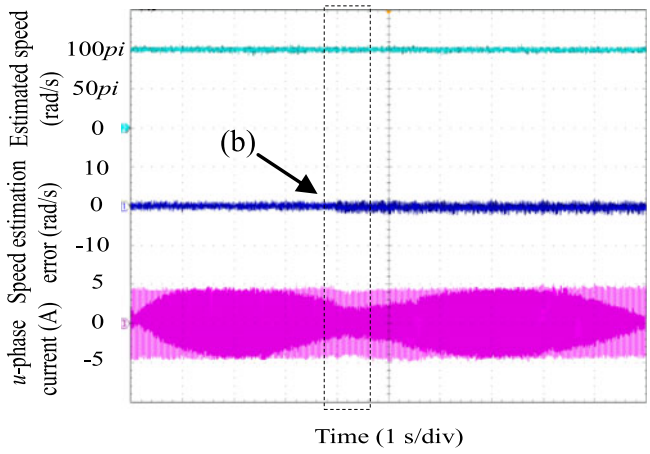

(a)

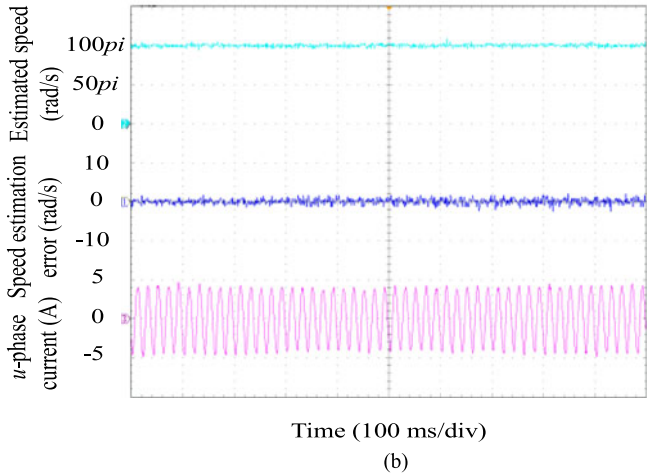

(b)

Fig. 14. Speed estimation performance based on MC-MM-EKF when speed-sensor fails at 100*pi* rad/s with 100% rated torque.

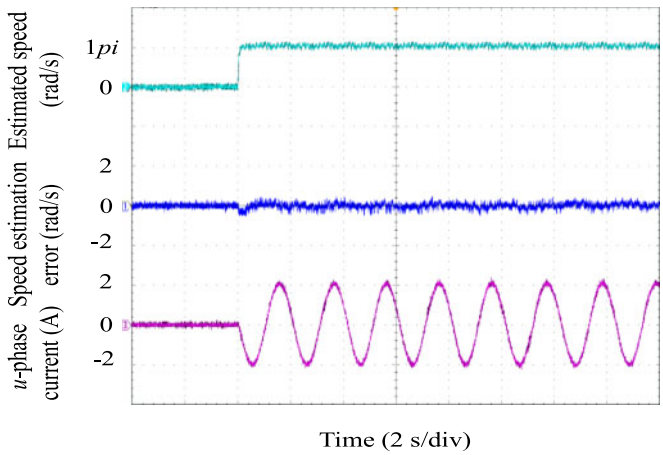

Fig. 15. Experimental results based on MC-MM-EKF at 1*pi* rad/s.

100% rated torque. The speed based on speed-sensor is used feedback speed before 4 s, and the speed based on MC-MM-EKF is used feedback speed after 4 s to simulate encoder failure. From the experimental results, the current waveform has slight oscillation, but it restores stability quickly and the motor can operate stably. Therefore, MC-MM-EKF is particularly suitable for the products of the speed-sensorless compact drives composing of a motor and an inverter, the applications such as electrical or hybrid vehicles, where both a resolver as speed sensor and a speed estimation algorithm which are used and required for safety purposes in case the speed-sensor fails.

Fig. 15 shows the estimated speed and the stator current based on MC-MM-EKF at 1*pi* rad/s. From top to bottom, the estimated

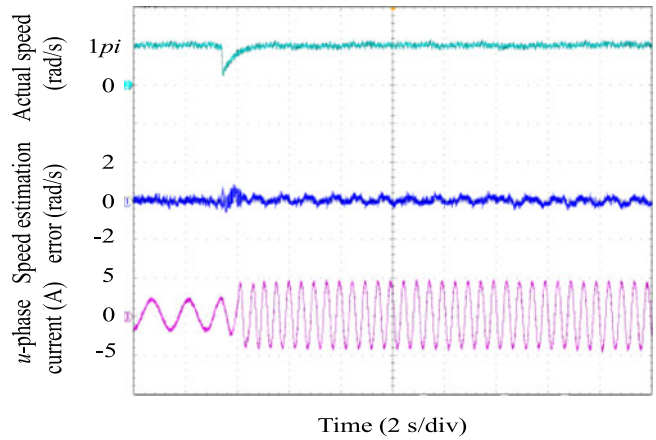

Fig. 16. Experimental results based on MC-MM-EKF at 1*pi* rad/s with step load from 0% to 100% rated torque.

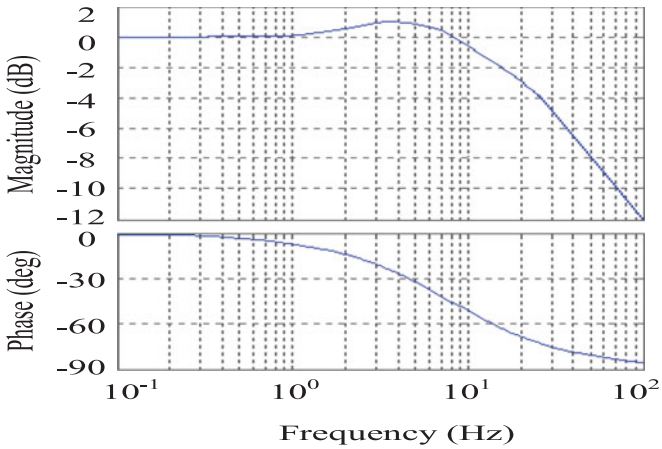

Fig. 17. Bode diagram of the speed loop.

speed, the speed estimation error, and the *u*-phase current are given, respectively. It can be seen that the stator current is close to sine, and the motor can operate stably at low speed.

Fig. 16 shows the experimental results based on MC-MM-EKF at 1*pi* rad/s with step load disturbance from 0% to 100% rated torque. From top to bottom, the rotor speed, the speed estimation error, and the *u*-phase current are given, respectively. It can be seen that the motor can run stably at low speed, and the motor speed can track the given speed again very soon when the load changes rapidly. Therefore, MC-MM-EKF has good dynamic performance against step load at low speed.

The frequency where 45 [°] phase delay occurs is considered as the bandwidth of the regulator in this paper. Fig. 17 shows the Bode plot of the speed loop. It can be seen that the bandwidth of the speed regulator is almost 8 Hz when phase delay is 45 [°]. Fig. 18 shows sine wave response of the speed loop at 8 Hz based on MC-MM-EKF, and the magnitude of the speed reference is 8*pi* rad/s. From top to bottom, the speed reference, the rotor speed, and the estimated speed are given, respectively. As shown in Fig. 18, the estimated speed is identical with the actual speed, and it can be concluded that the speed estimation based on MC-MM-EKF is performed quite well.

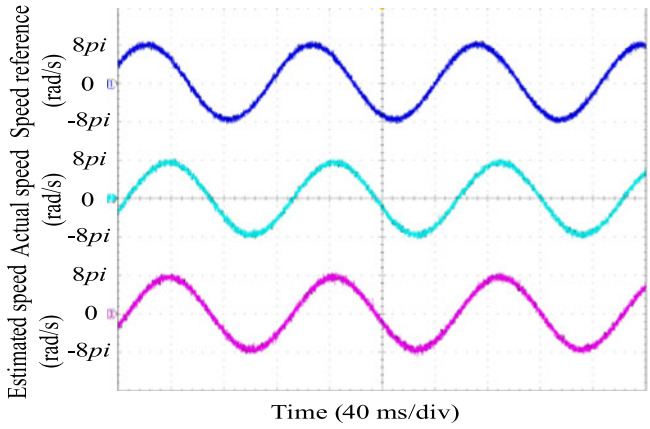

Fig. 18. Sine wave response of the speed loop at 8 Hz.

Figs. 13–18 demonstrate the correctness of the speed estimation system based on MC-MM-EKF.

Fig. 19 shows the speed response and the stator current based on EKF, IMM-EKF, and MC-MM-EKF when the given speed ranges from +100*pi* to –100*pi* rad/s. From top to bottom, the rotor speed, the estimated speed, the *u*-phase current, and the speed estimation error are given, respectively. Fig. 19(a) shows the experimental results based on EKF, Fig. 19(b) shows the experimental results based on IMM-EKF, and Fig. 19(c) shows the experimental results based on MC-MM-EKF. It indicates that in the process of the motor speed reversal, the current waveform has no oscillation and transition, and the estimated speed based on EKF, IMM-EKF, and MC-MM-EKF remains stable, and the smooth switching is achieved on zero-crossing position. However, the speed estimation error of EKF and IMM-EKF is larger than MC-MM-EKF in the process of the motor speed reversal.

Figs. 20, 21, and 22 show the response of the closed-loop system based on EKF, IMM-EKF, and MC-MM-EKF with no load. The initial given speed is 100*pi* rad/s, then the motor decelerates from 100*pi* to 2*pi* rad/s and accelerates from 2*pi* to 50*pi* rad/s at the speed slew rate of 25*pi* rad/s/s. Fig. 20 shows the estimated speed and the speed estimation error comparison with EKF, IMM-EKF, and MC-MM-EKF. From top to bottom, the estimated speed and the speed estimation error are given, respectively. Fig. 20(a) shows the experimental results based on EKF, Fig. 20(b) shows the experimental results based on IMM-EKF, and Fig. 20(c) shows the experimental results based on MC-MM-EKF. From the experimental results, all estimators have good steady performance, and the mean error is zero, but the fluctuation of EKF and IMM-EKF is larger than MC-MM-EKF. At the same time, MC-MM-EKF has better dynamic property than EKF and IMM-EKF in the motor acceleration and deceleration process. As shown in Fig. 21, EKF, IMM-EKF, and MC-MM-EKF can reproduce the current, but MC-MM-EKF has the best precision. Fig. 22 shows the estimated flux linkage comparison with EKF, IMM-EKF, and MC-MM-EKF. It can be seen that the estimated flux linkage based on EKF and IMM-EKF has a larger fluctuation, but the fluctuation based on MC-MM-EKF is rather small.

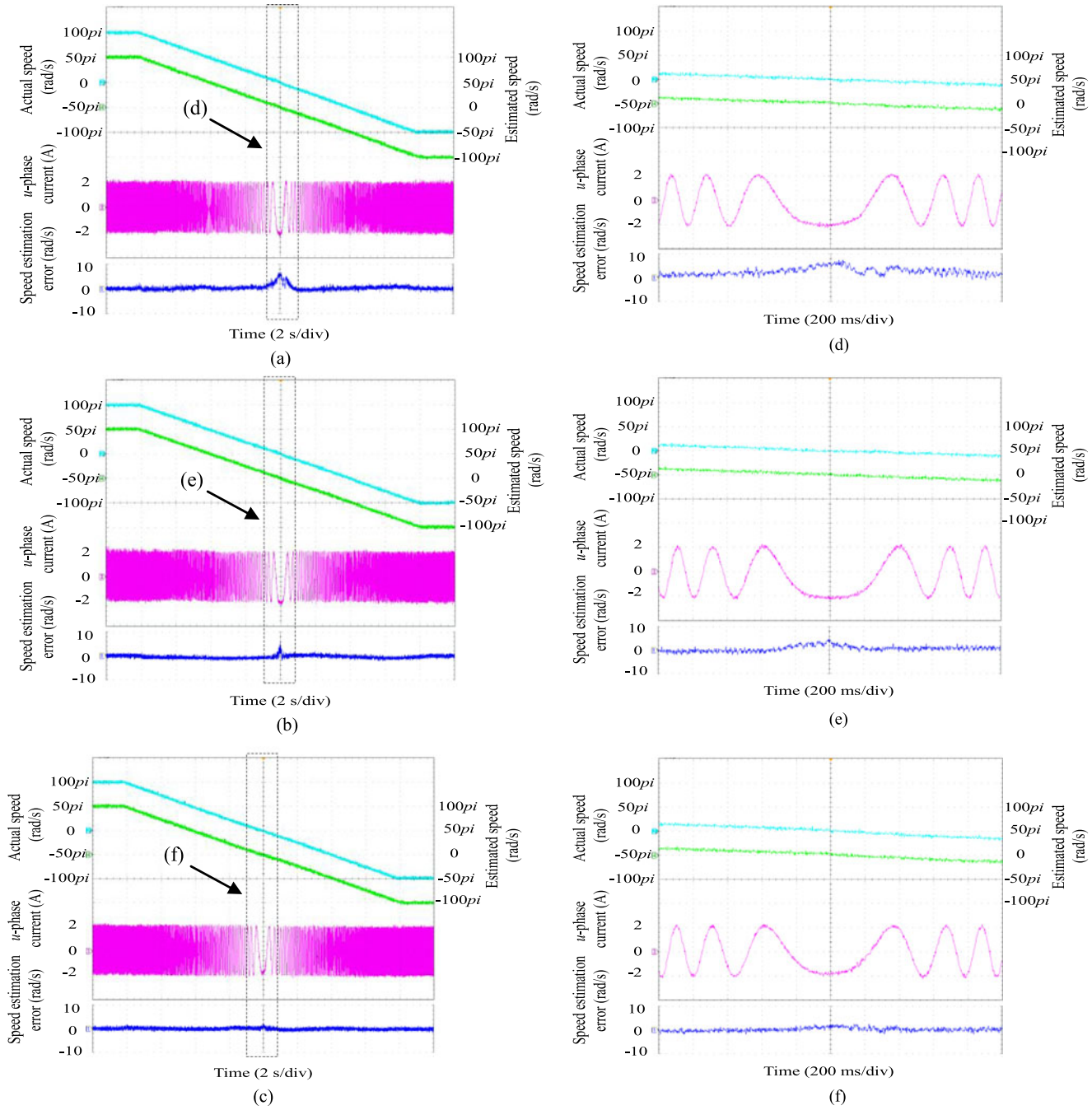

Fig. 19. Estimated speed and stator current at switching point of reversal. (a) EKF. (b) IMM-EKF. (c) MC-MM-EKF.

Figs. 20, 21, and 22 indicate the speed and flux estimation system based on MC-MM-EKF has better estimation performance than EKF and IMM-EKF in the whole speed range.

B. Robustness to Motor Parameter Variations

Fig. 24 shows the estimated speed and the speed estimation error of EKF, IMM-EKF, and MC-MM-EKF at 2*pi* rad/s with $1.3L_{\mathrm{m}}$. From top to bottom, the estimated speed and the speed estimation error are given, respectively. Fig. 24(a) shows the experimental results based on EKF, Fig. 24(b) shows the experimental results based on IMM-EKF, and Fig. 24(c) shows the experimental results based on MC-MM-EKF. From the experimental results, the estimated speed based on EKF has the largest fluctuation with mismatched L_{m}, and the maximum error of the speed estimation is 1.5 rad/s. The estimated speed based on IMM-EKF has larger fluctuation with mismatched L_{m}, and the maximum error of the speed estimation is 1.3 rad/s. The fluctuation of estimated speed based on MC-MM-EKF is rather small with mismatched L_{m}, and the maximum error of the speed estimation is 1 rad/s.

Fig. 25 shows the estimated speed and the speed estimation error of EKF, IMM-EKF, and MC-MM-EKF at 2*pi* rad/s

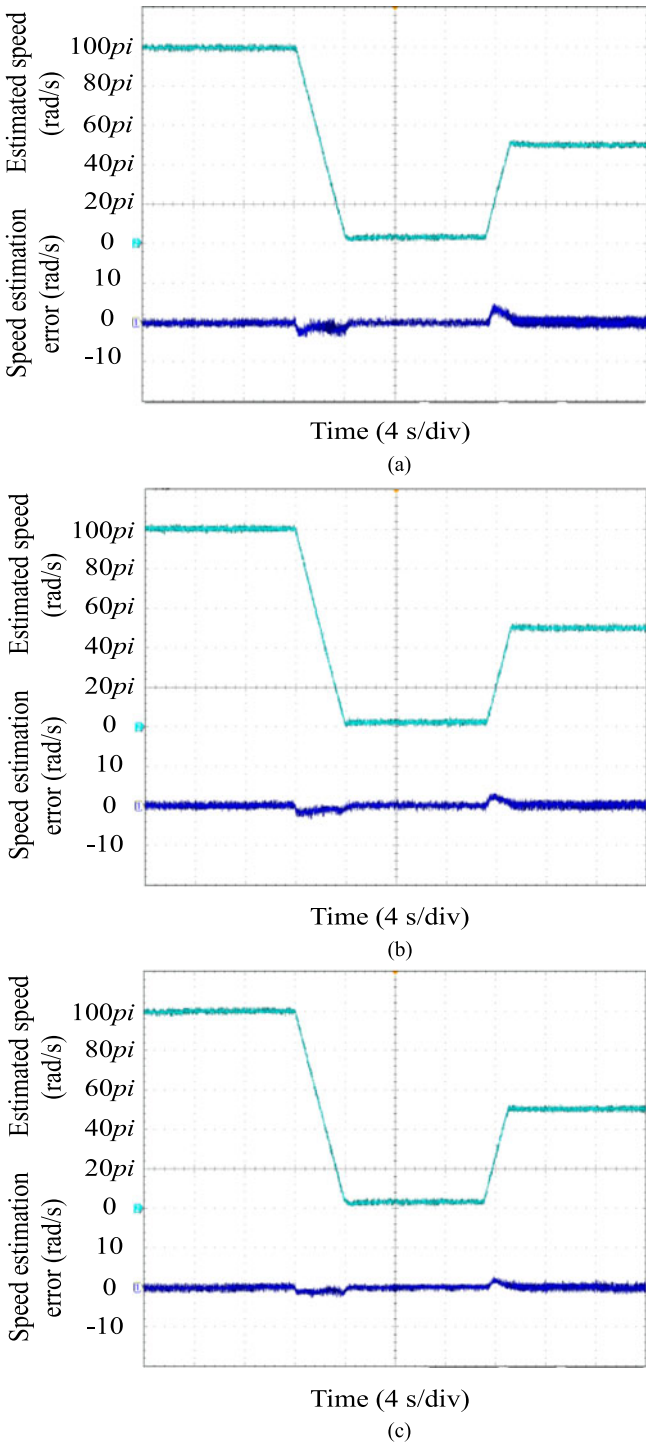

Fig. 20. Experimental comparison of the speed estimation error with no load. (a) EKF. (b) IMM-EKF. (c) MC-MM-EKF.

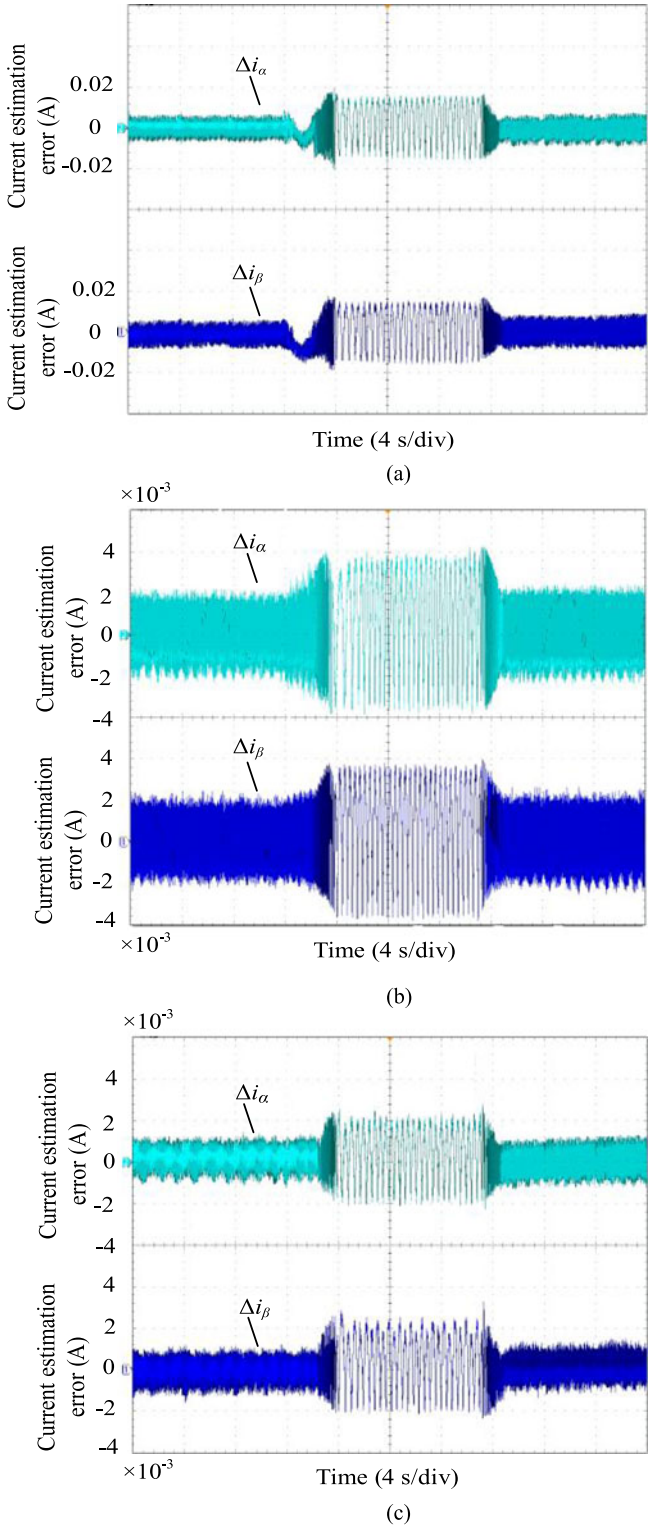

Fig. 21. Experimental comparison of the current estimation error with no load. (a) EKF. (b) IMM-EKF. (c) MC-MM-EKF.

with $1.3R_{r.}$ From top to bottom, the estimated speed and the speed estimation error are given, respectively. Fig. 25(a) shows the experimental results based on EKF, Fig. 25(b) shows the experimental results based on IMM-EKF, and Fig. 25(c) shows the experimental results based on MC-MM-EKF. It can be seen that the estimated speed based on EKF has the largest fluctuation with mismatched $R_{r.}$, and the maximum error of the speed estimation is 2 rad/s. The estimated speed based on IMM-EKF has larger fluctuation with mismatched $R_{r.}$, and the maximum error of the speed estimation is 1.6 rad/s. The estimated speed based on MC-MM-EKF is rather small with mismatched $R_{r.}$, and the maximum error of the speed estimation is 1.2 rad/s.

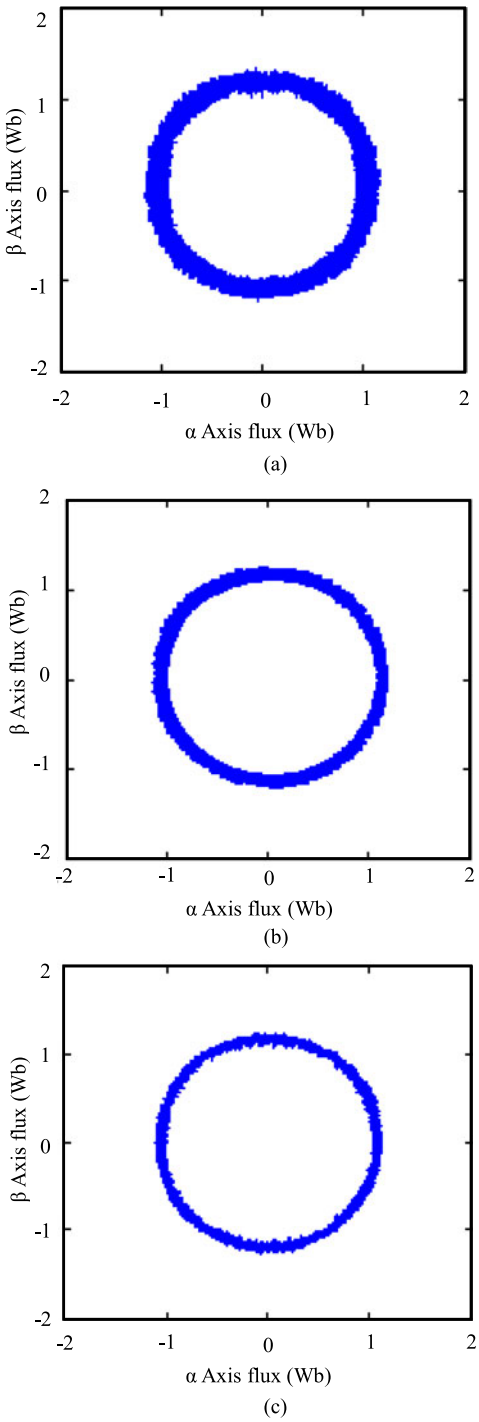

Fig. 22. Experimental comparison of the estimated flux linkage with no load. (a) EKF. (b) IMM-EKF. (c) MC-MM-EKF.

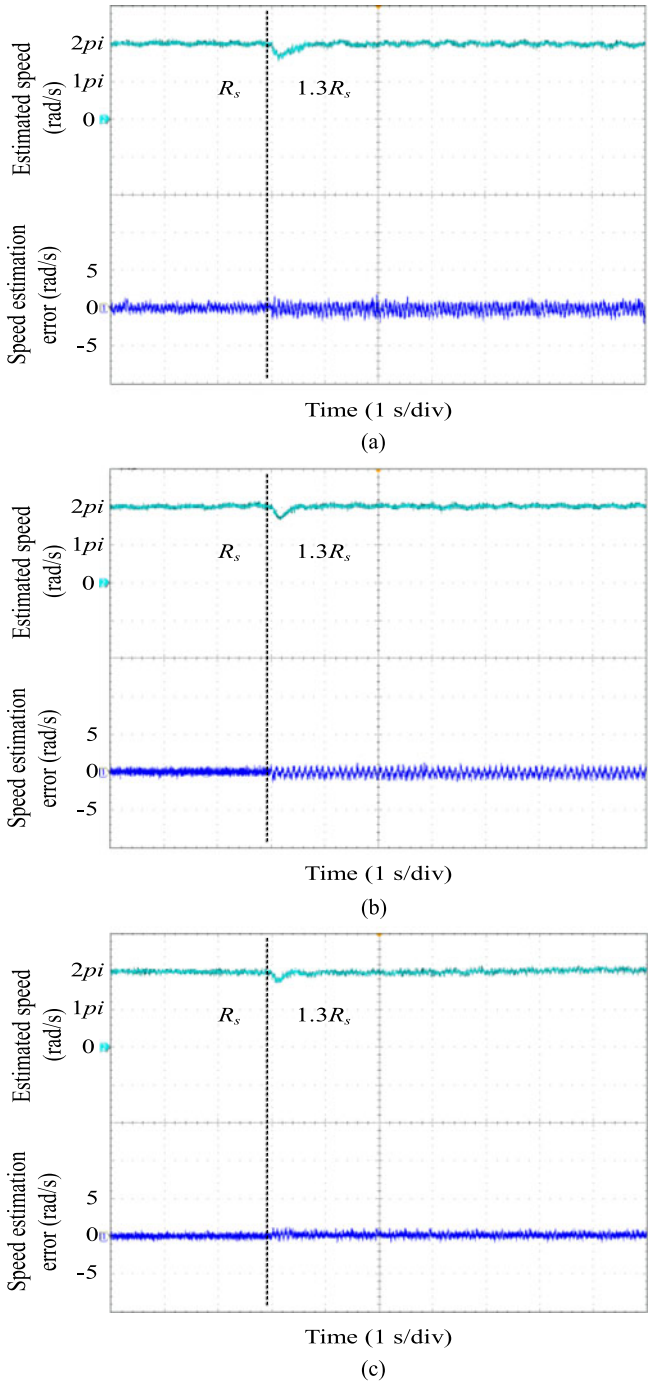

Fig. 23. Experimental comparison of the estimated speed and the speed estimation error at $2pi$ rad/s with $1.3R_s$. (a) EKF. (b) IMM-EKF. (c) MC-MM-EKF.

Figs. 23, 24, and 25 indicate that EKF is the most sensitive to the motor parameter variations, IMM-EKF is more sensitive to the motor parameter variations, and MC-MM-EKF has the best robustness to the motor parameter variations.

C. With Gross Estimation Error

Fig. 26 shows the estimated speed and the speed estimation error of EKF, IMM-EKF, and MC-MM-EKF when an error vector which is $[0\ 1\ 0\ 0\ 0]^{\mathrm{T}}$ is added to $\boldsymbol{x}$, and the given speed is $100pi$ rad/s. From top to bottom, the estimated speed and the speed estimation error are given, respectively. Fig. 26(a) shows the experimental results based on EKF, Fig. 26(b) shows the experimental results based on IMM-EKF, and Fig. 26(c) shows the experimental results based on MC-MM-EKF. It can be seen that the maximum fluctuation of the estimated speed based on EKF is 30 rad/s, and maximum error of the speed estimation is 12 rad/s. IMM-EKF has better anti-estimation-error ability, the maximum fluctuation of the estimated speed based on IMM-EKF

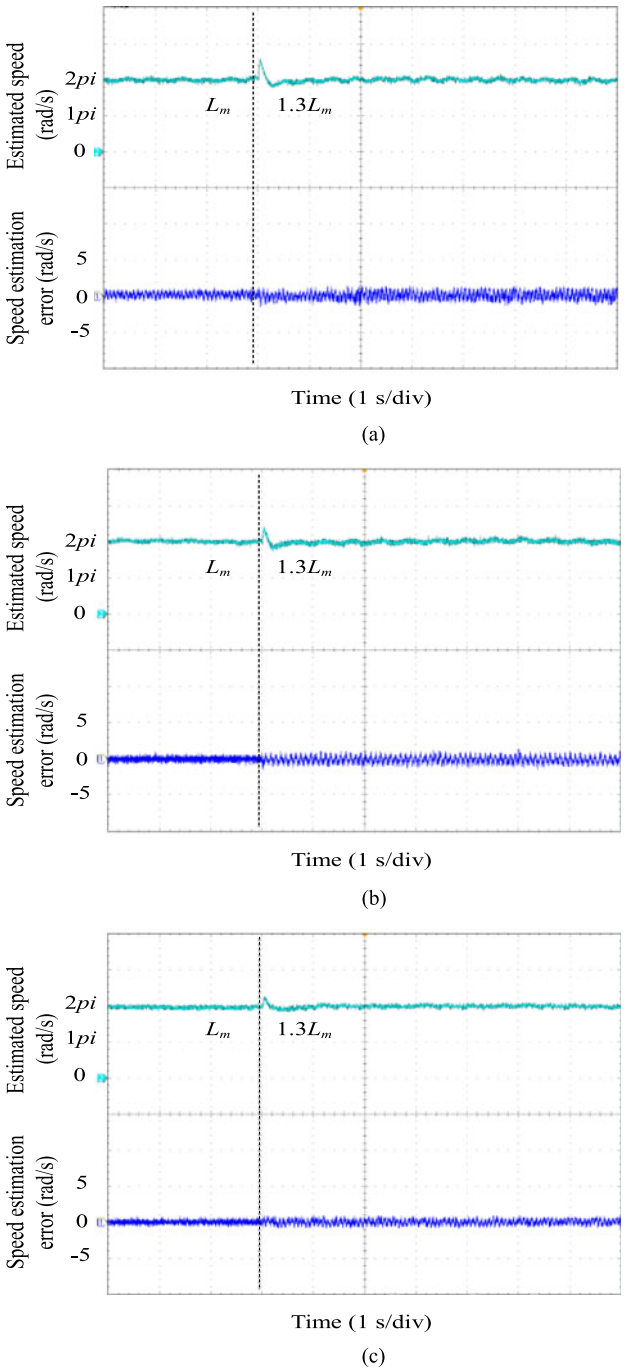

Fig. 24. Experimental comparison of the estimated speed and the speed estimation error at $2pi$ rad/s with $1.3L_{\mathrm{m}}$. (a) EKF. (b) IMM-EKF. (c) MC-MM-EKF.

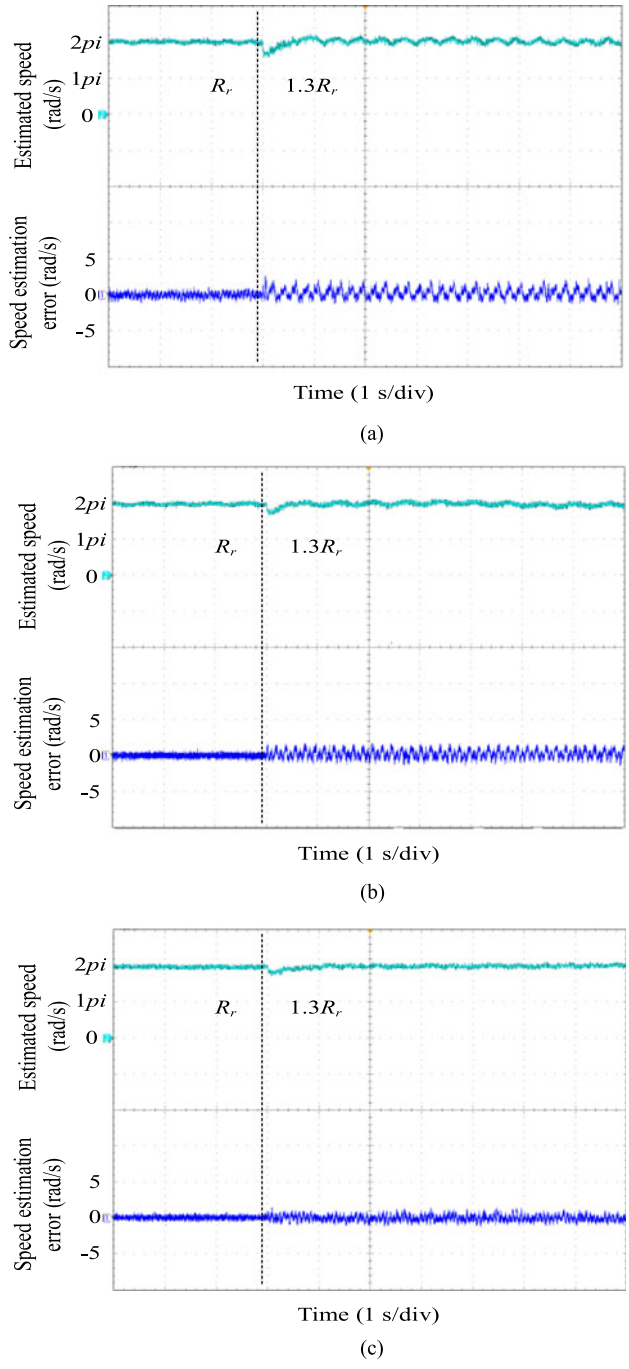

Fig. 25. Experimental comparison of the estimated speed and the speed estimation error at $2pi$ rad/s with $1.3R_{\mathrm{r}}$. (a) EKF. (b) IMM-EKF. (c) MC-MM-EKF.

is 19 rad/s, and the maximum error of the speed estimation is 8 rad/s. MC-MM-EKF has the best anti-estimation-error ability, the maximum fluctuation of the estimated speed based on IMM-EKF is 9 rad/s, and the maximum error of the speed estimation is 5 rad/s.

D. With Gross External Disturbance

In order to test the anti-error ability of MC-MM-EKF, a disturbance pulse which valued 2 A is added to the current detection channels by a signal generator when the given speed is $100pi$ rad/s. Fig. 27 shows the estimated speed and the speed estimation error of EKF, IMM-EKF, and MC-MM-EKF. From top to bottom, the estimated speed and the speed estimation error are given, respectively.Fig. 27(a) shows the experimental results based on EKF, Fig. 27(b) shows the experimental results based on IMM-EKF, and Fig. 27(c) shows the experimental results based on MC-MM-EKF. From the experimental results, the maximum fluctuation of the estimated speed based on EKF is 28 rad/s, and the maximum error of the speed estimation is 11 rad/s. IMM-EKF has better anti-error ability, the maxi-

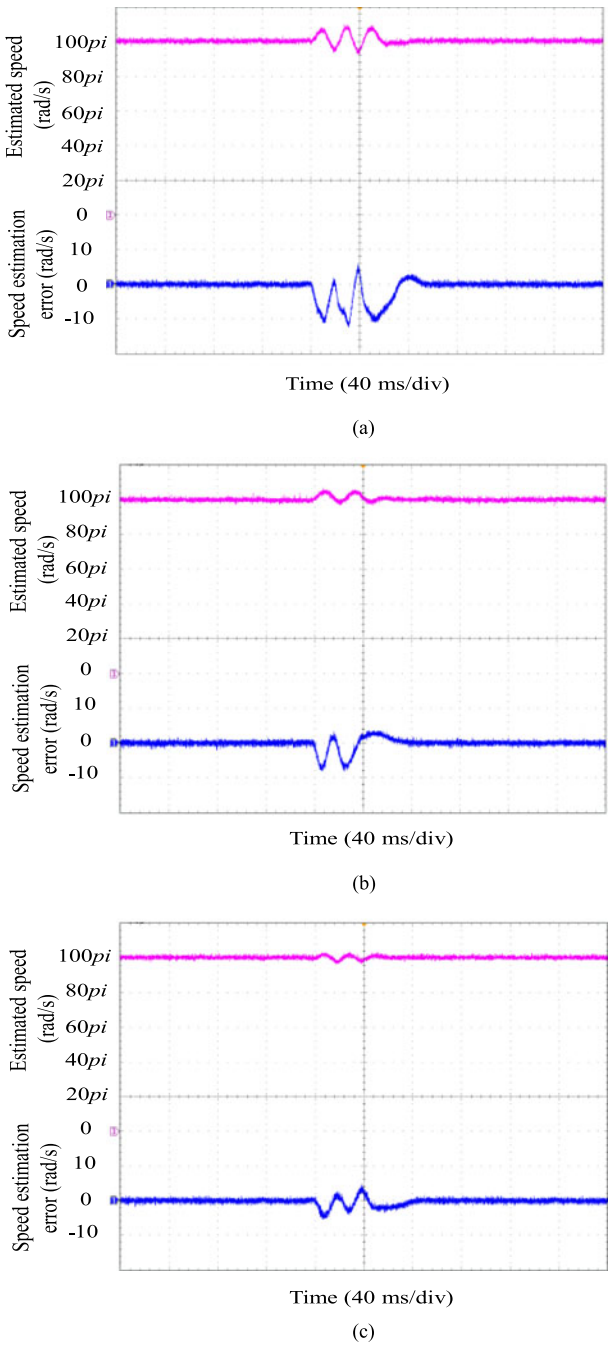

Fig. 26. Experimental comparison of the estimated speed and the speed estimation error at 100*pi* rad/s with gross estimation error. (a) EKF. (b) IMM-EKF. (c) MC-MM-EKF.

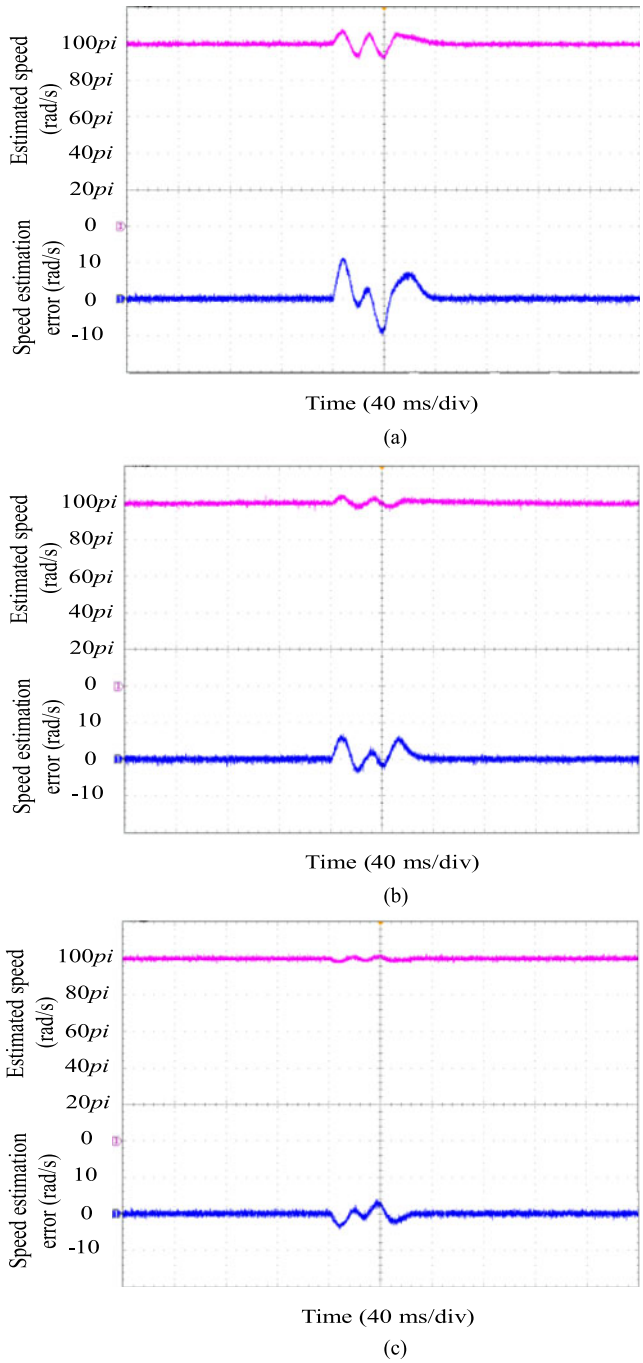

Fig. 27. Experimental comparison of the estimated speed and the speed estimation error at 100*pi* rad/s with gross external disturbance. (a) EKF. (b) IMM-EKF. (c) MC-MM-EKF.

mum fluctuation of the estimated speed based on IMM-EKF is 11 rad/s, and the maximum error of the speed estimation is 7 rad/s. MC-MM-EKF has the best anti-error ability, the maximum fluctuation of the estimated speed based on IMM-EKF is 4 rad/s, and the maximum error of the speed estimation is 4 rad/s.

E. Dynamic Performance Verification at Fast and Slow Speed Slew Rate With Load

Fig. 28 shows the speed estimation error comparison with EKF, IMM-EKF, and MC-MM-EKF at the slow speed acceleration and deceleration with 80% rated load, and the speed slew rate is 12*pi* rad/s/s. From top to bottom, the rotor speed, the estimated speed, and the speed estimation error are given, respectively. Fig. 28(a) shows the experimental results based on EKF, Fig. 28(b) shows the experimental results based on IMM-EKF, and Fig. 28(c) shows the experimental results based on MC-MM-EKF. It can be seen that the maximum error of speed estimation based on EKF is 5 rad/s at the speed slew rate of 12 rad/s/s, and the maximum error of

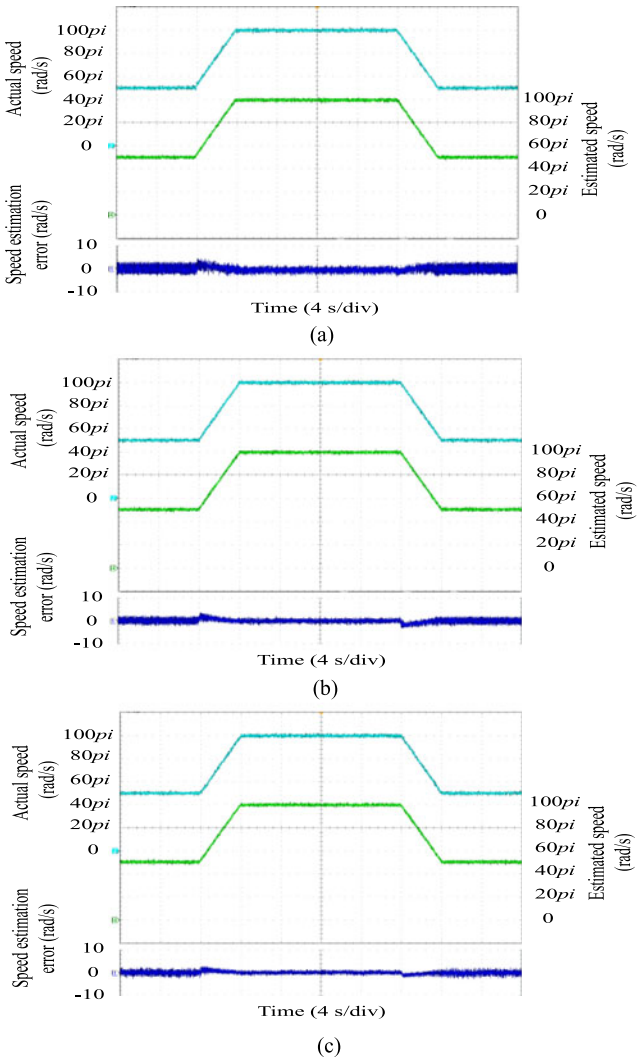

Fig. 28. Experimental comparison of the speed estimation error with the speed slew rate of 12 rad/s/s at deceleration and acceleration under 80% rated load. (a) EKF. (b) IMM-EKF. (c) MC-MM-EKF.

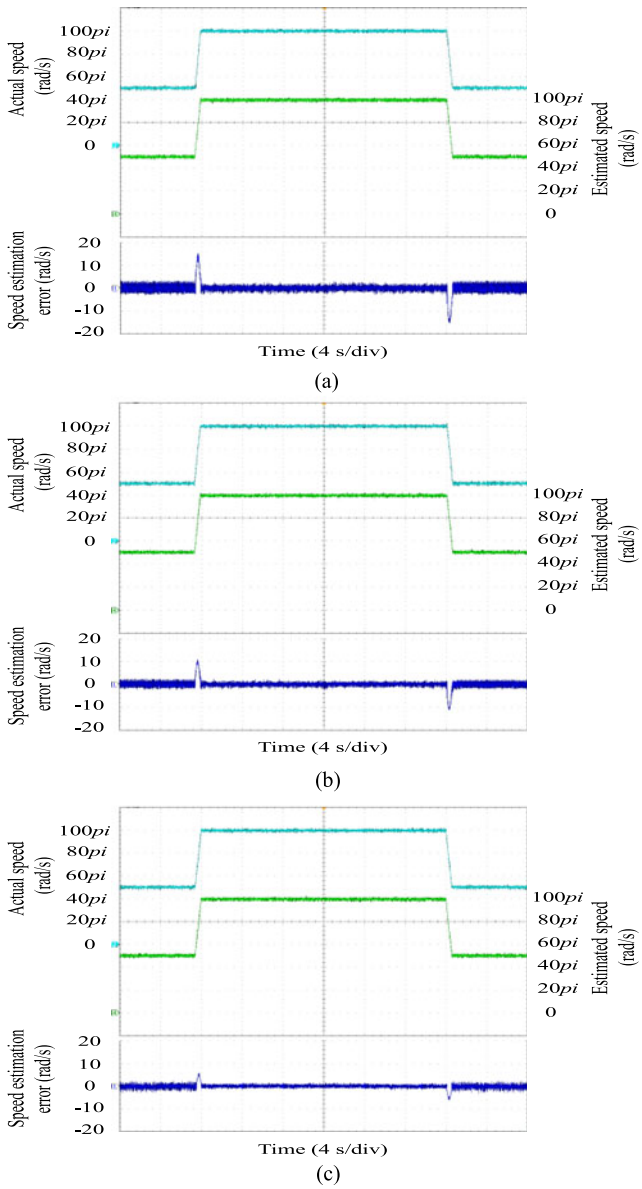

Fig. 29. Experimental comparison of the speed estimation error with the speed slew rate of 100*pi* rad/s/s at deceleration and acceleration under 80% rated load. (a) EKF. (b) IMM-EKF. (c) MC-MM-EKF.

speed estimation based on IMM-EKF is 3.7 rad/s. The speed estimation error obviously reduces based on MC-MM-EKF, and the maximum error of the speed estimation reduces to 2 rad/s.

Fig. 29 shows the speed estimation error comparison with EKF, IMM-EKF, and MC-MM-EKF at the fast speed acceleration and deceleration with 80% rated load, and the speed slew rate is 100*pi* rad/s/s. From top to bottom, the rotor speed, the estimated speed, and the speed estimation error are given, respectively. Fig. 29(a) shows the experimental results based on EKF, Fig. 29(b) shows the experimental results based on IMM-EKF, and Fig. 29(c) shows the experimental results based on MC-MM-EKF. The motor accelerates from 50*pi* to 100*pi* rad/s and then decelerates to 50*pi* rad/s. From the experimental results, the maximum error of speed estimation based on EKF is 15 rad/s at the speed slew rate of 100*pi* rad/s/s, and the maximum error of speed estimation based on IMM-EKF is 11 rad/s. The speed estimation error obviously reduces based on MC-MM-EKF, and the maximum error of the speed estimation reduces to 6 rad/s.

F. Dynamic Performance Verification with Step Load

Fig. 30 shows the speed estimation error comparison with EKF, IMM-EKF, and MC-MM-EKF at 100*pi* rad/s with step load disturbance from 0% to 100% rated torque. From top to bottom, the rotor speed, the estimated speed, the *u*-phase current, and the speed estimation error are given, respectively. Fig. 30(a) shows the experimental results based on EKF, Fig. 30(b) shows the experimental results based on IMM-EKF, and Fig. 30(c) shows the experimental results based on MC-MM-EKF. It can be seen that the maximum error of speed estimation based on EKF is 17 rad/s during the whole operation with step load disturbance, and the maximum error of speed estimation based on

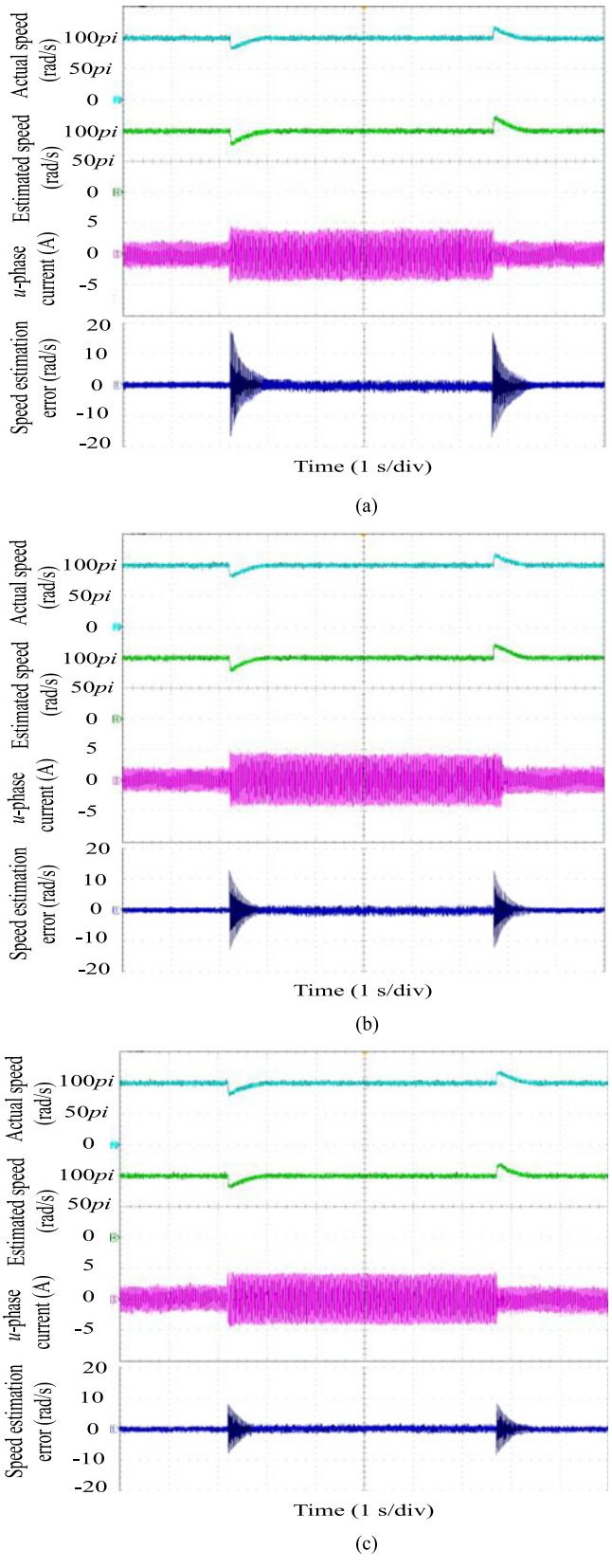

Fig. 30. Experimental comparison of the speed estimation error at 100*pi* rad/s with step load disturbance from 0% to 100% rated torque. (a) EKF. (b) IMM-EKF. (c) MC-MM-EKF.

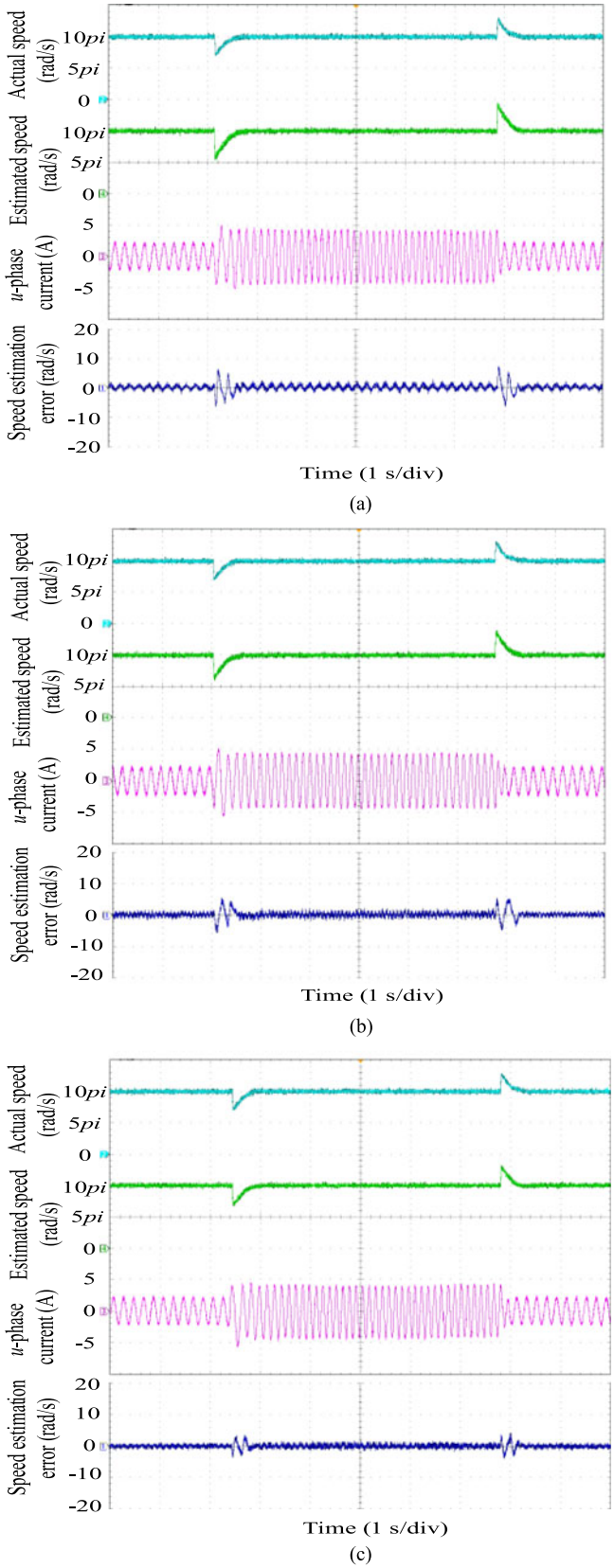

Fig. 31. Experimental comparison of the speed estimation error at 10*pi* rad/s with step load disturbance from 0% to 100% rated torque. (a) EKF. (b) IMM-EKF. (c) MC-MM-EKF.

IMM-EKF is 13 rad/s. The speed estimation error obviously reduces based on MC-MM-EKF during the whole operation with step load disturbance, and the maximum error of the speed estimation reduces to 9 rad/s. Therefore, MC-MM-EKF is effective for the sensorless control and has better dynamic tracking performance than EKF and IMM-EKF at high speed with step load.

Fig. 31 shows the speed estimation error comparison with EKF, IMM-EKF, and MC-MM-EKF at 10*pi* rad/s with step load disturbance from 0% to 100% rated torque. From top to bottom, the rotor speed, the estimated speed, the *u*-phase current, and the speed estimation error are given, respectively. Fig. 31(a) shows the experimental results based on EKF, Fig. 31(b) shows the experimental results based on IMM-EKF, and Fig. 31(c) shows the experimental results based on MC-MM-EKF. From the experimental results, the maximum error of speed estimation based on EKF is 7 rad/s during the whole operation with step load disturbance, and the maximum error of speed estimation based on IMM-EKF is 5.7 rad/s. The speed estimation error obviously reduces based on MC-MM-EKF during the whole operation with step load disturbance, and the maximum error of the speed estimation reduces to 4 rad/s. Therefore, MC-MM-EKF is effective for the sensorless control and has better dynamic tracking performance than EKF and IMM-EKF at low speed with step load.

VI. Conclusion

An adaptive speed estimation method for IMs based on MC-MM-EKF has been proposed in this paper. The correction and the effectiveness of the proposed method have been verified at an IM sensorless drive. The experimental results demonstrate that MC-MM-EKF can effectively improve the model adaptability to the actual systems and the environmental variations. The maximum error of the speed estimation with disturbance and motor parameter mismatches is obviously reduced, and both the steady and transient performance is improved by using the proposed adaptive speed estimation method. Moreover, compared with IMM-EKF, the real-time implementation of MC-MM-EKF is equivalent with it. Compared with other optimized algorithms, such as differential evolution algorithm, nondominated sorting genetic algorithm and particle swarm optimization, and the optimization process are executed off-line. Therefore, the real-time implementation of MC-MM-EKF is better than differential evolution algorithm, nondominated sorting genetic algorithm, and particle swarm optimization.

Appendix

In MC-MM-EKF, all EKF models work in parallel. The estimation value is obtained by mixing the outputs of different models in different weightings, and the sum of the weightings is one. The total output is linear with the output of every model, as long as every EKF model is convergent, and thus MC-MM-EKF observer can be convergent. Therefore, it is essential to prove the convergence of EKF. If *Q* and *R* are restrained appropriately, the sufficient conditions which ensure asymptotic convergence are established. The convergence analysis of EKF is proved as follows.

First, the state estimation error $\hat{\delta}_{k+1}$ and the state prediction error $\tilde{\delta}_{k+1}$ are defined by

$$\hat{\delta}_{k+1} = x_{k+1} - \hat{x}_{k+1} \tag{A-1}$$

$$\tilde{\delta}_{k+1} = x_{k+1} - \tilde{x}_{k+1}. \tag{A-2}$$

The candidate Lyapunov function M_{k+1} is as follows:

$$M_{k+1} = \hat{\delta}_k^T P_{k+1}^{-1} \hat{\delta}_k. \tag{A-3}$$

The aim is to determine conditions for which M_{k+1} is a decreasing sequence and to show EKF limitations when the first-order approximation is used, and e_{k+1} and $\tilde{\delta}_{k+1}$ are approximated as follows:

$$e_{k+1} = H_{k+1} \tilde{\delta}_{k+1} \tag{A-4}$$

$$\tilde{\delta}_{k+1} = G_k \hat{\delta}_k. \tag{A-5}$$

For a rigorous convergence study, it is shown that M_{k+1} decreases. There always exist residues, due to the first-order linearization technique, of every output error prediction component e_{k+1}^i of e_{k+1} and every state error prediction component $\tilde{\delta}_{k+1}^i$ of $\tilde{\delta}_{k+1}$, for all k. To take these residues into account, in order to obtain an exact equality, the unknown diagonal matrices α_{k+1} and β_{k+1} are introduced, and thus

$$H_{k+1}^i \tilde{\delta}_{k+1} = \alpha_{k+1}^i e_{k+1}^i \tag{A-6}$$

$$\tilde{\delta}_{k+1}^j = \beta_{k+1}^i G_k^j \hat{\delta}_k \tag{A-7}$$

$$\alpha_{k+1} e_{k+1} = H_{k+1} \tilde{\delta}_{k+1} \tilde{\delta}_{k+1} = \beta_{k+1} G_k \hat{\delta}_k \tag{A-8}$$

where $\alpha_{k+1} \in R^{p.p}$ and $\beta_{k+1} \in R^{n.n}$.

By subtracting both sides of $\hat{x}_{k+1} = \tilde{x}_{k+1} + K_{k+1} e_{k+1}$ from x_{k+1}, the following equation is obtained:

$$\hat{\delta}_{k+1} = \tilde{\delta}_{k+1} - \tilde{P}_{k+1} H_{k+1} \times \left(H_{k+1} \tilde{P}_{k+1} H_{k+1}^T + R_{k+1} \right)^{-1}. \tag{A-9}$$

From $K_{k+1} = \tilde{P}_{k+1} H_{k+1}^T (H_{k+1} \tilde{P}_{k+1} H_{k+1}^T + R_{k+1})^{-1}$ and $\hat{P}_{k+1} = (I - K_{k+1} H_{k+1}) \tilde{P}_{k+1}$, the following equations are obtained:

$$\hat{P}_{k+1} H_{k+1}^T R_{k+1}^{-1} = \tilde{P}_{k+1} H_{k+1}^T \left(H_{k+1} \tilde{P}_{k+1} H_{k+1}^T + R_{k+1} \right)^{-1} \tag{A-10}$$

$$\hat{P}_{k+1}^{-1} = \tilde{P}_{k+1}^{-1} + H_{k+1} R_{k+1}^{-1} H_{k+1}^T. \tag{A-11}$$

Substituting (A-10) into (A-9) and (A-9) into (A-3), the quadratic function becomes

$$M_{k+1} = (\tilde{\delta}_{k+1} - \hat{P}_{k+1} H_{k+1}^T R_{k+1}^{-1} e_{k+1})^T \bullet \hat{P}_{k+1}^{-1} (\tilde{\delta}_{k+1} - \hat{P}_{k+1} H_{k+1}^T R_{k+1}^{-1} e_{k+1}) \tag{A-12}$$

or

$$\begin{aligned} M_{k+1} = \; & \tilde{\delta}_{k+1}^T \hat{P}_{k+1}^{-1} \tilde{\delta}_{k+1} - \tilde{\delta}_{k+1}^T H_{k+1}^T R_{k+1}^{-1} e_{k+1} \\ & - e_{k+1}^T R_{k+1}^{-1} H_{k+1} \tilde{\delta}_{k+1} \\ & \times e_{k+1}^T R_{k+1}^{-1} H_{k+1} \hat{P}_{k+1} H_{k+1}^T R_{k+1}^{-1} e_{k+1}. \end{aligned} \tag{A-13}$$

Substituting (A-11) into (A-13)

$$\begin{aligned} M_{k+1} = \; & \tilde{M}_{k+1} + \tilde{\delta}_{k+1}^T H_{k+1}^T R_{k+1}^{-1} H_{k+1} \tilde{\delta}_{k+1} \\ & - \tilde{\delta}_{k+1}^T H_{k+1}^T R_{k+1}^{-1} e_{k+1} + e_{k+1}^T R_{k+1}^{-1} H_{k+1} \tilde{\delta}_{k+1} \\ & + e_{k+1}^T R_{k+1}^{-1} H_{k+1} \hat{P}_{k+1} H_{k+1}^T R_{k+1}^{-1} e_{k+1} \end{aligned} \tag{A-14}$$

with

$$\tilde{M}_{k+1} = \tilde{\delta}_{k+1}^T \tilde{P}_{k+1}^{-1} \tilde{\delta}_{k+1}. \tag{A-15}$$

From (A-6) and (A-7), (A-14) becomes

$$\begin{aligned} M_{k+1} = \; & \tilde{M}_{k+1} + e_{k+1}^T \Big(\alpha_{k+1} R_{k+1}^{-1} \alpha_{k+1} \\ & - \alpha_{k+1} R_{k+1}^{-1} - R_{k+1}^{-1} \alpha_{k+1} \\ & + R_{k+1}^{-1} H_{k+1} \hat{P}_{k+1} H_{k+1}^T R_{k+1}^{-1} \Big) e_{k+1}. \end{aligned} \tag{A-16}$$

On the other hand, $\tilde{M}_{k+1}$ can be written as follows:

$$\tilde{M}_{k+1} = \hat{\delta}_k^T G_k^T \beta_k (G_k \hat{P}_k G_k^T)^{-1} \beta_k G_k \hat{\delta}_k. \tag{A-17}$$

A decreasing sequence $\{M_{k+1}\}$ means that

$$M_{k+1} - M_k = M_{k+1} - \tilde{M}_{k+1} + \tilde{M}_{k+1} - M_k \leq 0 \tag{A-18}$$

or equivalently

$$\begin{aligned} M_{k+1} - M_k = \; & e_{k+1}^T (\alpha_{k+1} R_{k+1}^{-1} \alpha_{k+1} - \alpha_{k+1} R_{k+1}^{-1} \\ & - R_{k+1}^{-1} \alpha_{k+1} + R_{k+1}^{-1} H_{k+1} \hat{P}_{k+1} \\ & H_{k+1}^T R_{k+1}^{-1}) e_{k+1} + \hat{\delta}_k^T G_k^T \beta_k (G_k \hat{P}_k G_k^T)^{-1} \\ & \beta_k G_k \hat{\delta}_k. \end{aligned} \tag{19}$$

The sufficient conditions which ensures asymptotic convergence are

$$\begin{aligned} & e_{k+1}^T (\alpha_{k+1} R_{k+1}^{-1} \alpha_{k+1} - \alpha_{k+1} R_{k+1}^{-1} - R_{k+1}^{-1} \alpha_{k+1} \\ & + R_{k+1}^{-1} H_{k+1} \hat{P}_{k+1} H_{k+1}^T R_{k+1}^{-1}) e_{k+1} \leq 0 \end{aligned} \tag{A-20}$$

and

$$\hat{\delta}_k^T G_k^T \beta_k (G_k \hat{P}_k G_k^T)^{-1} \beta_k G_k \hat{\delta}_k \leq 0. \tag{A-21}$$

Before we give sufficient conditions to ensure the convergence of EKF, two lemmas are established for intermediate results.

Lemma 1: Assuming that every α_{k+1}^i satisfies the following condition:

$$1 - \sqrt{1 - \Delta_{k+1}} \leq \alpha_{k+1}^i \leq 1 + \sqrt{1 - \Delta_{k+1}} \tag{A-22}$$

$$\begin{aligned} \Delta_{k+1} = \; & \lambda_{\max}(R_{k+1}) \lambda_{\max}(R_{k+1}^{-1} H_{k+1} \tilde{P}_{k+1} H_{k+1}^T \\ & \bullet (H_{k+1} \tilde{P}_{k+1} H_{k+1}^T + R_{k+1})^{-1}) \end{aligned} \tag{A-23}$$

where $\lambda_{\max}()$ represents the maximum eigenvalue and R_{k+1} is chosen such that $\Delta_{k+1} \leq 1$, then (A-20) is verified.

Lemma 2: Assuming that

$$G_k i \text{ s a bounded nonsingular matrix} \tag{A-24}$$

and every β_k^j satisfies the following condition:

$$-1 \leq \beta_k^j \leq 1. \tag{A-25}$$

Then, (A-21) is verified.

The convergence of EKF is not ensured even if M_{k+1} is a decreasing sequence. Therefore, some additional conditions in relation to the reconstructibility are needed. Under (A-24), if there exist positive real numbers η_1 and η_2 so that for all $k \geq N$ and for some finite $N \geq 0$, and thus

$$\eta_1 I_n \leq O_e^T(N,k) \Re(k-N,k) O_e(k-N,k) \leq \eta_2 I_n \tag{A-26}$$

$$O_e(k-N,k) = \begin{bmatrix} H_{k-N} G_{k-N}^{-1} G_{k-N+1}^{-1} \cdots G_{k-1}^{-1} \\ H_{k-N+1} G_{k-N+1}^{-1} \cdots G_{k-1}^{-1} \\ \vdots \\ H_k \end{bmatrix} \tag{A-27}$$

$$\Re(k-N,k) = \operatorname{diag}(R_{k-N}^{-1}, \cdots, R_k^{-1}). \tag{A-28}$$

According to (A-26), the following lemma can be obtained.

Lemma 3: If we assume that state equations are reconstructible by (A-26), then we have

$$\lim_{k \to \infty} \lambda_{\min}(\hat{P}_k^{-1}) = \infty \tag{A-29}$$

and

$$\operatorname{Sup} \lim_{k \to \infty} \frac{\lambda_{\max}[\hat{P}_k^{-1}]}{\lambda_{\min}[\hat{P}_k^{-1}]}. \tag{A-30}$$

Theorem: Based on (A-22), (A-24), (A-25), and (A-26), then EKF used as an observer for the nonlinear discrete-time system is ensured that

$$\lim_{k \to \infty} (x_k - \hat{x}_k) = \lim_{k \to \infty} \hat{\delta}_k = 0. \tag{A-31}$$

Proof: Based on (A-22) and (A-25), it has been shown (according to Lemmas 1 and 2) that $\{M_{k+1}\}$ is a decreasing sequence which converges to a positive scalar M

$$\lim_{k \to \infty} M_k = M. \tag{A-32}$$

On the other hand

$$\frac{M_k}{tr(\hat{P}_k^{-1})} \geq \frac{\lambda_{\min}[\hat{P}_k^{-1}] \hat{\delta}_k^T \hat{\delta}_k}{n \lambda_{\max}[\hat{P}_k^{-1}]} \tag{A-33}$$

where *tr*() is the trace of matrix.

According to (A-29), it can be obtained

$$\lim_{k\to\infty} tr(\hat{P}_k^{-1}) = \infty. \tag{A-34}$$

Then

$$\frac{\lambda_{\min}[\hat{P}_k^{-1}]\hat{\delta}_k^T\hat{\delta}_k}{n\lambda_{\max}[\hat{P}_k^{-1}]} = 0. \tag{A-35}$$

According to (A-30), it can be obtained

$$\lim_{k\to\infty} \hat{\delta}_k = 0. \tag{A-36}$$

The convergence of EKF can be proved by the above method. By restraining Q and R appropriately, the convergence of MC-MM-EKF also can be ensured.

REFERENCES

[1] X. Sun, L. Chen, Z. Yang, and H. Zhu, "Speed-sensorless vector control of a bearingless induction motor with artificial neural network inverse speed observer," *IEEE Trans. Mechatronics*, vol. 18, no. 4, pp. 1357–1366, Aug. 2013.

[2] T. Orlowska-Kowalska and M. Dybkowski, "Stator-current-based MRAS estimator for a wide range speed-sensorless induction-motor drive," *IEEE Trans. Ind. Electron.*, vol. 57, no. 4, pp. 1296–1308, Apr. 2010.

[3] M. O. Sonnaillon, G. Bisheimer, C. De Angelo, and G. O. García, "Online sensorless induction motor temperature monitoring," *IEEE Trans. Energy Convers.*, vol. 25, no. 2, pp. 273–280, Jun. 2010.

[4] S. Maiti and C. Chakraborty, "An alternative adaptation mechanism for model reference adaptive system based sensorless induction motor drive," *Elect. Power Comput. Syst.*, vol. 38, no. 6, pp. 710–736, Apr. 2010.

[5] C. Caruana, G. M. Asher, and M. Sumner, "Performance of HF signal injection techniques for zero-low-frequency vector control of induction machines under sensorless conditions," *IEEE Trans. Ind. Electron.*, vol. 53, no. 1, pp. 225–238, Feb. 2006.

[6] J. Holtz, "Sensorless control of induction machines—With or without signal injection," *IEEE Trans. Ind. Electron.*, vol. 53, no. 1, pp. 7–30, Feb. 2006.

[7] S. Po-ngam and S. Sangwongwanich, "Stability and dynamic performance improvement of adaptive full-order observers for sensorless PMSM drive," *IEEE Trans. Power Electron.*, vol. 27, no. 2, pp. 588–600, Feb. 2012.

[8] G.-H. Xi, H.-Y. Gao, W. Xu, S.-Y. Yu, and W.-H. Gui, "A method to determine gain matrix of stator flux full order observer," *J. Central South Univ. (Sci. Technol.)*, vol. 39, no. 4, pp. 793–798, 2008.

[9] M. S. Zaky, "Stability analysis of speed and stator resistance estimators for sensorless induction motor drives," *IEEE Trans. Ind. Electron.*, vol. 59, no. 2, pp. 858–870, Feb. 2012.

[10] X. Zhang, "Sensorless induction motor drive using indirect vector controller and sliding-mode observer for electric vehicles," *IEEE Trans. Veh. Technol.*, vol. 62, no. 7, pp. 3010–3018, Sep. 2013.

[11] M. Ghanes and G. Zheng, "On sensorless induction motor drives: Sliding-mode observer and output feedback controller," *IEEE Trans. Ind. Electron.*, vol. 56, no. 9, pp. 3404–3413, Sep. 2013.

[12] M. Barut, R. Demir, E. Zerdali, and R. Inan, "Real-time implementation of bi input-extended Kalman filter-based estimator for speed-sensorless control of induction motors," *IEEE Trans. Ind. Electron.*, vol. 59, no. 11, pp. 4197–4206, Nov. 2012.

[13] X. Xiao and C. Chen, "Dynamic permanent magnet flux estimation of permanent magnet synchronous machines," *IEEE Trans. Appl. Supercond.*,vol. 20, no. 3, pp. 1085–1088, Jun. 2010.

[14] M. Barut, S. Bogosyan, and M. Gokasan, "Experimental evaluation of braided EKF for sensorless control of induction motors," *IEEE Trans. Ind. Electron.*, vol. 55, no. 2, pp. 620–632, Feb. 2008.

[15] M. Bendjedia, Y. Ait-Amirat, B. Walther, and A. Berthon, "Position control of a sensorless stepper motor," *IEEE Trans. Power Electron.*, vol. 27, no. 2, pp. 578–587, Feb. 2012.

[16] Z. G. Yin, C. Zhao, J. Liu, and Y. R. Zhong, "Research on anti-error performance of speed and flux estimator for induction motor using robust reduced-order EKF," *IEEE Trans. Ind. Inform.*, vol. 9, no. 2, pp. 1037–1046, May 2013.

[17] L. Ke and X. Jian, "Strong track Schmidt filter and its application to speed sensorless control of induction motor," *ACTA Autom. Sin.*, vol. 34, no. 9, pp. 1076–1082, 2008.

[18] M. Barut, S. Bogosyan, and M. Gokasan, "EKF based sensorless direct torque control of IMs in the low speed range," in *Proc. Conf. IEEE Int. Symp. Ind. Electron.*, Dubrovnik, Croatia, 2005, pp. 969–974.

[19] R. N. Andriamalala, H. Razik, J. N. Razafinjaka, L. Baghli, and F. Sargos, "Independent and direct rotor-flux oriented control of series-connected induction machines using decoupled Kalman-filters," in *Proc. 37th Annu. IEEE Conf. Ind. Electron. Soc.*, Melbourne, Australia, 2011, pp. 3488–3494.

[20] I. M. Alsofyani and N. R. N. Idris, "Simple flux regulation for improving state estimation at very low and zero speed of a speed sensorless direct torque control of an induction motor," *IEEE Trans. Power. Electron.*, vol. 31, no. 4, pp. 3027–3035, Apr. 2016.

[21] Y. Chinniah, R. Burton, and S. Habibi, "Failure monitoring in a high performance hydrostatic actuation system using the extended Kalman filter," *Mechatronics*, vol. 16, pp. 643–653, 2006.

[22] B. Akin, U. Orguner, A. Ersak, and M. Ehsani, "Simple derivative-free nonlinear state observer for sensorless AC drives," *IEEE/ASME Trans. Mechatronics*, vol. 11, no. 5, pp. 634–643, Oct. 2006.

[23] B. Akin, U. Orguner, A. Ersak, and M. Ehsani, "A comparative study on non-linear state estimators applied to sensorless ac drives MRAS and Kalman filter," in *Proc. 34th Annu. Conf. IEEE Ind. Electron. Soc.*, 2004, vol. 3, pp. 2148–2153.

[24] Y. Liu, Z. Q. Zhu, and D. Howe, "Instantaneous torque estimation in sensorless direct-torque-controlled brushless DC motors," *IEEE Trans. Ind. Appl.*, vol. 42, no. 5, pp. 1275–1283, Sep./Oct. 2006.

[25] N. Salvatore, A. Caponio, F. Neri, S. Stasi, and G. L. Cascella, "Optimization of delayed-state Kalman-filter-based optimization of delayed-state Kalman-filter-based control of induction motors," *IEEE Trans. Ind. Electron.*, vol. 57, no. 1, pp. 385–394, Jan. 2010.

[26] T. Schuhmann and W. Hofmann, "Improving operational performance of active magnetic bearings using Kalman filter and state feedback control," *IEEE Trans. Ind. Electron.*, vol. 59, no. 2, pp. 821–829, Feb. 2012.

[27] M. Habibullah and D. D. C. Lu, "A speed-sensorless FS-PTC of induction motors using extended Kalman filters," *IEEE Trans. Ind. Electron.*, vol. 62, no. 11, pp. 6765–6778, Nov. 2015.

[28] Z. G. Yin, C. Zhao, J. Liu, and Y. R. Zhong, "Research on robust performance of speed-sensorless vector control for the induction motor using an interfacing multiple-model extended Kalman filter," *IEEE Trans. Power Electron.*, vol. 29, no. 6, pp. 3011–3019, Jun. 2014.

[29] K. Szabat, T. Orlowska-Kowalska, and M. Dybkowski, "Indirect adaptive control of induction motor drive system with an elastic coupling," *IEEE Trans. Ind. Electron.*, vol. 56, no. 10, pp. 4038–4042, Oct. 2009.

[30] M. Hilairet, F. Auger, and E. Berthelot, "Speed and rotor flux estimation of induction machines using a two-stage extended Kalman filter," *Automatica*, vol. 45, no. 8, pp. 1819–1827, Aug. 2009.

[31] F. Alonge, T. Cangemi, F. D'Ippolito, A. Fagiolini, and A. Sferlazza, "Convergence analysis of an extended Kalman filter for sensorless control of induction motors," *IEEE Trans. Ind. Electron.*, vol. 62, no. 4, pp. 2341–2352, Apr. 2015.

[32] M. Barut, S. Bogosyan, and M. Gokasan, "Speed-sensorless estimation for induction motors using extended Kalman filters," *IEEE Trans. Ind. Electron.*, vol. 54, no. 1, pp. 272–280, Feb. 2007.

[33] F. Alonge and F. D'Ippolito, "Robustness analysis of an extended Kalman filter for sensorless control of induction motors," in *Proc. IEEE Int. Symp. Ind. Electron.*, 2010, pp. 3257–3263.

[34] N. Salvatore, A. Caponio, F. Neri, S. Stasi, and G. L. Cascella, "Optimization of delayed-state Kalman-filter-based optimization of delayed-state Kalman-filter-based control of induction motors," *IEEE Trans. Ind. Electron.*, vol. 57, no. 1, pp. 385–394, Jan. 2010.

[35] M. Boussak, "Implementation and experimental investigation of sensorless speed control with initial rotor position estimation for interior permanent magnet synchronous motor drive," *IEEE Trans. Power Electron.*, vol. 20, no. 6, pp. 1413–1422, Nov. 2005.

[36] D. Efimov, A. Zolghadri, and P. Simon, "Improving fault detection abilities of extended Kalman filters by covariance matrices adjustment," in *Proc. Conf. Control Fault Tolerant Syst.*, Nice, France, Oct. 2010, pp. 131–136.

[37] S. Jafarzadeh, C. Lascu, and M. S. Fadali, "State estimation of induction motor drives using the unscented Kalman filter," *IEEE Trans. Ind. Electron.*, vol. 59, no. 11, pp. 4207–4216, Nov. 2012.

Zhonggang Yin (M'13) was born in Shandong, China, in 1982. He received the B.S., M.S., and Ph.D. degrees in electrical engineering from the Xi'an University of Technology, Xi'an, China, in 2003, 2006, and 2009, respectively.

In 2009, he joined the Electrical Engineering Department, Xi'an University of Technology, where he is currently an Associate Professor. His research interests include high-performance control of ac motor, and digital control of power converters.

Guoyin Li was born in Chongqing, China, in 1992. He received the B.S. degree in electrical engineering, in 2014, from the Xi'an University of Technology, Xi'an, China, where he is currently working toward the M.S. degree in power electronics and electrical drives in electrical engineering.

His research interests include high-performance control of ac motor.

Yanqing Zhang was born in Shaanxi, China, in 1989. He received the B.S. and M.S. degrees in electrical engineering, in 2012 and 2015, respectively, from the Xi'an University of Technology, Xi'an, China, where he is currently working toward the Ph.D. degree in electrical engineering.

His research interests include high-performance control of ac motor.

Jing Liu was born in Anhui, China, in 1982. She received the B.S., M.S., and Ph.D. degrees in electronic engineering from the Xi'an University of Technology, Shaanxi, China, in 2003, 2006, and 2009, respectively.

In 2009, she joined the Electronic Engineering Department, Xi'an University of Technology, where she is currently an Associate Professor. Her research interests include the power semiconductor devices and their application to power electronic devices.

Xiangdong Sun was born in Shenyang, China, in 1971. He received the Ph.D. degree in electrical engineering from the Xi'an University of Technology, Xi'an, China, in 2003. He did the postdoctoral research in Tokyo Polytechnic University, Tokyo, Japan, supported by the government scholarship of Japan during 2006–2008.

He is a Professor in the Department of Electrical Engineering, Xi'an University of Technology. His research interests include motor control, power electronics, and renewable energy system.

Yanru Zhong was born in Xi'an, China, in 1950. He received the B.S. degree in electrical engineering from Xi'an Jiaotong University, Xi'an, China, in 1975, and the M.S. degree in electrical engineering from the Xi'an University of Technology, Xi'an, in 1983.

He joined the Xi'an University of Technology in 1983. He was a Visit Scholar in the Electrical Engineering Department, Sophia University, Tokyo, Japan, in 1987. Since 1993, he has been a Professor with Xi'an University of Technology. His research interests include power electronics, especially inverter and ac drive systems.